Icarus 409 (2024) 115847

Contents lists available at ScienceDirect

Icarus

journal homepage: www.elsevier.com/locate/icarus

Research Paper

3D Monte-Carlo simulation of Ganymede's atmosphere

Audrey Vorburger [a,b,*], Shahab Fatemi [b], Shane R. Carberry Mogan [c], André Galli [a], Lucas Liuzzo [c], Andrew R. Poppe [c], Lorenz Roth [d], Peter Wurz [a]

[a] Physics Institute, University of Bern, Bern, Switzerland
[b] Department of Physics, University of Umeå, Umeå, Sweden
[c] Space Sciences Laboratory, University of California, Berkeley, CA, USA
[d] Division of Space and Plasma Physics, KTH Royal Institute of Technology, Stockholm, Sweden

ARTICLE INFO

Keywords:
Ganymede
Atmosphere
Sputtering
Sublimation
Monte-Carlo model

ABSTRACT

We present new model results for H_2O, O_2, H_2, O, and H in the atmosphere of Ganymede. The results are obtained from a collision-less 3D Monte-Carlo model that includes sublimation, ion and electron sputtering, and ion and electron radiolysis. Because Ganymede has its own magnetic field, its immediate plasma environment is particularly complex. The interaction between Ganymede's and Jupiter's magnetospheres makes it highly variable in both space and time. The recent Juno Ganymede flyby provided us with new data on the electron local environment. Based on the electron measurements recorded by the Jovian Auroral Distributions Experiment (JADE), we implement two electron populations, one for the moon's polar regions and one for the moon's auroral regions. Comparing the atmospheric contribution of these newly defined electron populations to the overall source and loss processes is one of the main goals of this work.

Our analysis shows that for H_2O, sublimation remains the most important source process even after accounting for the new electron populations, delivering more than three orders of magnitude more H_2O molecules to the atmosphere than all other source processes combined. The source fluxes for O_2 and H_2, on the other hand, are dominated by radiolysis induced by the auroral electrons, assuming that the electron fluxes JADE measured during Juno's transit of Ganymede's magnetopause current layer are representative of auroral electrons. Atomic O and H are mainly added to the atmosphere through the dissociation of O_2 and H_2, which is primarily induced by auroral electrons.

Our understanding of Ganymede's atmosphere today is mainly based on spectroscopic observations. The interpretation of spectroscopic data strongly depends on assumptions taken, though. Our analysis shows that for a holistic understanding of Ganymede's atmosphere, simultaneous observations of the moon's surface, atmosphere, and full plasma environment (thermal and energetic ions and electrons) at different times and locations (both with respect to Ganymede and with respect to Jupiter) are particularly important. Such measurements are planned by ESA's Jupiter ICy moons Explorer (JUICE), in particular by the Particle Environment Package (PEP), which will greatly advance our understanding of Ganymede and its atmosphere and plasma environment.

1. Introduction

Ganymede's atmosphere is one of the most complex among the moons of our solar system. As the only known satellite in our solar system to feature an intrinsic global magnetic field (e.g., Gurnett et al., 1996; Kivelson et al., 2002), Ganymede forms a small magnetosphere within the much larger magnetosphere of Jupiter. The interaction of the two magnetic fields strongly influences the morphology of Ganymede's atmosphere and shapes the observed atmospheric auroral emissions (Hall et al., 1998; Feldman et al., 2000; McGrath et al., 2004; Saur et al., 2015; Musacchio et al., 2017; Molyneux et al., 2018; de Kleer et al., 2023).

The chemical composition of Ganymede's atmosphere directly reflects the chemical composition of its surface that primarily consists of water–ice (e.g., Ligier et al., 2019), much like the surfaces of the other icy Galilean satellites, Europa and Callisto (Pilcher et al., 1972; Clark and McCord, 1980; Calvin and Clark, 1991; Showman and Malhotra, 1999; Hansen and McCord, 2004; Moore et al., 2004). H_2O related-products thus comprise the main species in Ganymede's atmosphere. These products include H_2O molecules, non-condensing O_2 and H_2

---

* Corresponding author at: Physics Institute, University of Bern, Bern, Switzerland.
E-mail address: audrey.vorburger@unibe.ch (A. Vorburger).

https://doi.org/10.1016/j.icarus.2023.115847
Received 28 April 2023; Received in revised form 19 October 2023; Accepted 26 October 2023

molecules, as well as highly reactive dissociation products such as O, H, and OH. H_2O molecules can be liberated from Ganymede's surface and fed into its atmosphere through sputtering (i.e., the ejection of particles from a solid surface due to the surface being bombarded by energetic particles) and sublimation (i.e., the phase transition from a solid to a gaseous state) (see e.g., Vorburger et al., 2022). Sputtering closely follows the spatial distribution of the precipitating Jovian plasma, which is mainly governed by the interaction between Ganymede's internal magnetic field and the Jovian magnetic field (Fatemi et al., 2016; Poppe et al., 2018; Plainaki et al., 2020). Sublimation is strongly temperature-dependent, with the H_2O vapor pressure exhibiting an exponential correlation with surface temperature, which ranges on Ganymede from ~80 K to ~150 K, though maximum temperatures much lower than the 150 K have also been proposed (e.g., Spencer, 1987; Orton et al., 1996). O_2 and H_2 are produced through irradiation (i.e., the bombardment of Ganymede's surface by the energetic Jovian plasma ions and electrons) and diffuse out of the surface in time. O, H, and OH are also formed as a result of surface irradiation, but since they are chemically extremely reactive, they usually recombine within the ice without being given the chance to leave the ice via diffusion. Instead, these species are primarily created within the atmosphere through the dissociation of parent molecules (mainly H_2O, O_2, and H_2; see e.g., Turc et al., 2014).

Species in Ganymede's atmosphere inferred from observations include O_2, O, H, and H_2O (Barth et al., 1997; Hall et al., 1998; Feldman et al., 2000; McGrath et al., 2013; Saur et al., 2015; Alday et al., 2017; Musacchio et al., 2017; Molyneux et al., 2018; Roth et al., 2021; de Kleer et al., 2023; Leblanc et al., 2023). All of these observations are based on line emissions in the UV and optical range. Inferring the underlying atmospheric density from UV and optical line emissions is challenging, though. First, contributions by sources not associated with Ganymede's atmosphere have to be correctly removed; second, the remaining emission has to be correctly converted to atmospheric abundances. The latter requires excellent knowledge of the low-energy electron environment and photon flux, which are the main inducers of, for example, the oxygen line emissions, but which are not only temporally but also spatially highly variable (e.g., Kivelson et al., 2004). What further complicates matters is the fact that the cross sections of the different reactions are not known equally well. While, for example, the cross sections for electrons reacting with O_2 are established quite well, information on electrons reacting with H_2O is still sparse (see e.g., the discussion on this in McConkey et al., 2008).

Ganymede's electron environment has to be measured *in situ* or with radio-occultation techniques to obtain detailed information on its properties (i.e., spatial distribution and energy spectrum). Unfortunately, for the times of the available atmospheric spectroscopic observations, no such measurements exist. Thus, while these measurements present the current best constraints on Ganymede's atmosphere, the derived results depend heavily on the assumptions made by the respective authors. In the following two subsections, detailed information on the available observations is given, before previously published modeling efforts on Ganymede's atmosphere are reviewed. Section 2 then presents our modeling approach, the results of which are presented and discussed in detail in Section 3. Section 4 finally summarizes the main findings of the work presented herein.

1.1. Observations

Ganymede's atmosphere consists of a local (i.e., in the vicinity of the subsolar point), near-surface sublimated water atmosphere, a global, near-surface oxygen atmosphere and an extended global hydrogen corona (see references in the following paragraphs). Ganymede's atmospheric oxygen-containing species produce airglow emissions that closely follow the boundary between open and closed field lines, indicating that electrons precipitate along the open field lines to locally excite atmospheric oxygen (e.g., Hall et al., 1998; McGrath et al., 2013). The following paragraphs present the currently available observations of Ganymede's hydrogen, oxygen, and water atmosphere, while Table 1 summarizes the atmospheric densities and column densities inferred from aforementioned observations.

Hydrogen. The first positive evidence of an atmosphere at Ganymede was presented by Barth et al. (1997), who observed Lyman-α radiation from atomic hydrogen (H) above Ganymede's limb using the Galileo Ultraviolet Spectrometer (UVS). The observations were best reproduced by a hydrogen corona model with a surface density of $1.5 \cdot 10^4$ cm^{-3}, a column density of $9.2 \cdot 10^{12}$ cm^{-2}, and a scale height of one Ganymede radius (i.e., 2634 km). As possible source mechanisms, the authors cite photon-dissociation of sublimated H_2O vapor, photo-desorption of surface water–ice (either as H_2O followed by photon-dissociation or directly as H), and sputtering of water–ice by Jupiter's magnetospheric plasma (directly as H). These Lyman-α emission observations were later confirmed by Feldman et al. (2000), who detected Lyman-α emissions consistent with the Barth et al. (1997) measurements using the HST Space Telescope Imaging Spectrograph (STIS). In 2017, Alday et al. (2017) presented an analysis of 9 HST-STIS Lyman-α observations (3 of the trailing hemisphere and 6 of the leading hemisphere) acquired during four campaigns in 1998, 2000, 2011, and 2014. For the observations taken in 1998, 2000, and 2011, the authors derive relatively stable H surface densities of $(5–8) \cdot 10^3$ cm^{-3} (with a mean of $6.4 \cdot 10^3$ cm^{-3}). In the 2014 observations, however, the brightness of Ganymede's corona was much fainter, being ~3 times lower on the trailing hemisphere and hardly detectable on the leading hemisphere. One suggested explanation for these much lower values compared to the previous years' observations is extinction of Ganymede's corona signal in Earth's upper atmosphere or geocorona. The authors state that they refrain from a detailed discussion of the potential hydrogen density decrease due to the campaign's limited number of exposures that can be combined to improve the signal-to-noise ratio. They do point out, however, that Molyneux et al. (2017) also observed lower intensities in later OI 1304 Å and OI 1356 Å measurements compared to earlier measurements, suggesting different magnetospheric plasma conditions in Ganymede's vicinity at different times. Finally, Alday et al. (2017) state that their surface densities are consistent with the Feldman et al. (2000) observations and approximately two times lower than the surface densities inferred by Barth et al. (1997). The difference in density between the Galileo (earlier) and HST (later) observations might indicate a non-uniform distribution of Ganymede's hydrogen corona, a change in the hydrogen corona over time (1996 versus 1998–2014), or might be caused by the different instruments and analysis techniques.

Very recently, Roth et al. (2023) analyzed H Lyman-α images taken when Ganymede was in transit of Jupiter with HST-STIS. They found that the Jovian day-glow is attenuated by the H corona and derive similar densities as Alday et al. (2017) with the complementary observing technique. It is noteworthy that the similarities with Callisto's atmosphere suggest that H_2 may be the source of the observed atomic H, and not sublimated H_2O as previously thought (Carberry Mogan et al., 2022). Moreover, such a suggestion is also consistent with the recent Juno flyby that detected H_3^+ (Allegrini et al., 2022), which is produced via known chemical pathways in Ganymede's H_2 atmosphere.

Oxygen. The first Ganymede atmospheric oxygen measurements were published in 1998, when Hall et al. (1998) presented HST Goddard High Resolution Spectrograph (GHRS) OI 1304 & OI 1356 Å airglow observations of Ganymede's trailing hemisphere. The measured 1356 Å/1304 Å flux ratio of roughly 1–2 is diagnostic of dissociative electron impact excitation of O_2. Using an emission model that considers exospheric O and O_2 as possible constituents, Hall et al. (1998) derive O_2 column densities of $(1–10) \cdot 10^{14}$ cm^{-2} and an upper limit for the atomic O column density of $<3.5 \cdot 10^{13}$ cm^{-2}. Hall et al. (1998) furthermore note that the OI 1356 Å feature exhibits a double-peaked profile, i.e., two distinct and spatially confined emission regions consistent with the satellite's north and south poles, raising the possibility that polar aurorae may exist on Ganymede. A year later, Brown and Bouchez (1999) confirm the existence of atomic oxygen emission lines near the satellite's poles using Keck telescope data, but do not provide

Table 1
Inferred surface densities and column densities for the water-related species observed in Ganymede's atmosphere.

Species	N_0 [cm^{-3}]	NC [cm^{-2}]	Instrument	Observation	Comment	Reference
H	1.5e4	9.2e12	Galileo/UVS	Lyman-α	–	Barth et al. (1997)
	(5–8)e3	(1.5–2.2)e12	HST/STIS+COS	Lyman-α	leading & trailing hemispheres	Alday et al. (2017)
		(1–2)e12	HST/STIS	Lyman-α	anti-Jovian hemisphere	Roth et al. (2023)
O_2		(1–10)e14	HST/GHRS	OI 1304 Å & 1356 Å	trailing hemisphere	Hall et al. (1998)
	1e8	(0.3–5.2)e14	HST/STIS	OI 1304 Å & 1356 Å	–	Feldman et al. (2000)
		(4.7 ± 0.1)e14	Keck/HIRES	OI 5577–8446 Å	sub-Jovian hemisphere	de Kleer et al. (2023)
		(3.6–4.3)e14	HST/STIS	OI 1304 Å & 1356 Å	trailing and leading hemisphere, modeling	Leblanc et al. (2023)
O		<3.5e13	HST/GHRS	OI 1304 Å & 1356 Å	trailing hemisphere	Hall et al. (1998)
		(4–37)e12	HST/STIS+COS	OI 1304 Å & 1356 Å	trailing hemisphere; disk average	Molyneux et al. (2018)
		(6–60)e12	HST/STIS+COS	OI 1304 Å & 1356 Å	trailing hemisphere; auroral region	Molyneux et al. (2018)
		<2e12	HST/STIS+COS	OI 1304 Å & 1356 Å	sub-Jovian hemisphere	Roth et al. (2021)
		<3e13	Keck/HIRES	OI 5577–8446 Å	sub-Jovian hemisphere	de Kleer et al. (2023)
H_2O	≥1.2e9		HST/STIS+COS	OI 1304 Å & 1356 Å	trailing hemisphere average	Roth et al. (2021)
	≥2.0e8		HST/STIS+COS	OI 1304 Å & 1356 Å	leading hemisphere average	Roth et al. (2021)
		several 1e15	HST/STIS+COS	OI 1304 Å & 1356 Å	dayside average	Roth et al. (2021)
		<3e13	Keck/HIRES	OI 5577–8446 Å	sub-Jovian hemisphere	de Kleer et al. (2023)
		5.6e14–1.3e15	HST/STIS	OI 1304 Å & 1356 Å	trailing and leading hemisphere, modeling	Leblanc et al. (2023)

further details. Presenting 8 HST-STIS observations of Ganymede's trailing hemisphere in the spectral range 1160 Å –1720 Å, citeFeldman2000 confirmed the unambiguous existence of polar (latitudes above 40°) auroral emissions, stating that these are the result of dissociative electron impact excitation of O_2. The authors further state that they observed orbit-to-orbit variations and longitudinal non-uniformities in the emission brightness at high latitudes, which is suggestive of a variability that is correlated with changes in emission morphology. Eviatar et al. (2001) further shed light onto the processes that result in the auroral emissions, finding that (i) the location of the auroral ovals coincides with the location of the open-closed field line boundary in HST and Galileo observations and that (ii) ambient electrons are insufficient to generate the observed aurora and therefore must be locally accelerated in Ganymede's auroral regions. Further in-depth analyses of the auroral intensities and morphologies are presented in McGrath et al. (2013), Saur et al. (2015), Musacchio et al. (2017), Molyneux et al. (2018), which show that there are hemispheric dichotomies in the emission brightness (leading hemisphere > trailing hemisphere and sub-Jovian hemisphere > anti-Jovian hemisphere) and that the auroral oval appears quite stable on a multiyear time-scale but shows significant brightness fluctuations on a short time-scale. These variations are correlated with the strong interaction between Jupiter's magnetospheric plasma and Ganymede's mini-magnetosphere inside the current sheet, though, and do thus not imply underlying atmospheric variations. However, one observation by Molyneux et al. (2018) does suggest atmospheric differences, namely the observation that while the OI 1356 Å emission is consistently brighter on the leading hemisphere than on the trailing hemisphere, the emission of OI 1304 Å is similarly bright on both hemispheres, implying that while O_2 makes up >99% of the leading hemisphere atmosphere, the trailing hemisphere requires an atomic oxygen fraction of ~10%. Out of all the aforementioned papers, only Molyneux et al. (2018) derive number densities for the underlying atomic oxygen atmosphere, namely an O column density of (4.4–60)$\cdot 10^{12}$ cm^{-2} for the trailing hemisphere. In 2021, Roth et al. (2021) reported on sensitive spectra of Ganymede's auroral oxygen emissions with HST-COS during an eclipse passage in order to investigate the high O abundances proposed in earlier studies. They found a stable relative brightness of the OI 1356 Å and OI 1304 Å emissions when the moon enters eclipse, which rules out resonant solar scattering and thereby sets an upper limit for the atomic oxygen abundance of NC(O) $<2\cdot 10^{12}$ cm^{-2}. Furthermore, Marzok et al. (2022) derived a global map of the OI 1356 Å emissions, showing that the emission brightness varies along the ovals with minima near the sub- and anti-Jovian points, likely due to the lower electron precipitation in these regions, though Juno observations could not confirm this statement, not seeing much brightness variation in longitude with Juno's ultraviolet spectrograph (UVS) (Greathouse et al., 2022). Most recently, de Kleer et al. (2023) and Leblanc et al. (2023) both reported on spectroscopic observations of Ganymede's atmosphere, though conducted by different telescopes and at different wavelengths. While de Kleer et al. (2023) observed the optical aurora of Ganymede with Keck-HIRES, deriving O_2 column densities of (4.7 ± 0.1)$\cdot 10^{14}$ cm^{-2}, Leblanc et al. (2023) observed Ganymede's UV emissions with HST-STIS (similar to Roth et al., 2023), deriving O_2 column densities of (3.6–4.3)$\cdot 10^{14}$ cm^{-2}.

Water. In 2021, Roth et al. (2021) presented the first observational evidence for a sublimated water atmosphere on Ganymede acquired by HST-STIS. This evidence is based on OI 1356 Å/OI 1304 Å line emission ratios, which are at the disk center equal to 0.97 ± 0.22 and 1.83 ± 0.16 on the trailing and leading hemispheres, respectively. These values imply that in addition to the dominant O_2 component an additional, OI ratio reducing, atmospheric component is present. Through modeling, Roth et al. (2021) determine the O_2, O, and H_2O surface and column densities that best reproduce the measured OI line emission ratios. Their analysis yields maximum H_2O surface densities of $1.2\cdot 10^9$ cm^{-3} and $2.0\cdot 10^8$ cm^{-3} on the trailing and leading hemispheres, respectively, and a H_2O column density of several 10^{15} cm^{-2} in the subsolar region. Furthermore, Roth et al. (2023) looked at HST-STIS Lyman-α images taken in July 2021, and derived first upper limits for localized (plume) H_2O column densities at Ganymede of (2–3)$\cdot 10^{16}$ cm^{-2}. Very recently, de Kleer et al. (2023) and Leblanc et al. (2023) also looked for H_2O signatures in their respective aforementioned measurements. While Leblanc et al. (2023) derive H_2O column densities of $5.6\cdot 10^{14}$ cm^{-2} to $1.3\cdot 10^{15}$ cm^{-2}, agreeing with Roth et al. (2023), de Kleer et al. (2023) derive H_2O column densities of $<3\cdot 10^{13}$ cm^{-2}. As Leblanc et al. (2023) though states, the much lower value inferred by de Kleer et al. (2023) can be attributed to the fact that de Kleer et al. (2023) measured globally integrated emission ratios, which are only representative of the region near and above the limb, whereas the H_2O is mainly confined to the disk center, and thus remains undetected in their data.

1.2. Previous models

Previously published modeling efforts on Ganymede's atmosphere have predominantly concentrated on Ganymede's water-related atmosphere (Marconi, 2007; Turc et al., 2014; Plainaki et al., 2015; Shematovich, 2016; Leblanc et al., 2017; Vorburger et al., 2022; Leblanc et al., 2023). Whereas the different modeling efforts put emphasis on clearly distinct aspects of Ganymede's atmosphere (see below), they all agree on its general morphology: Up to a subsolar latitude of ~45°, H_2O dominates the atmospheric density, while elsewhere on the dayside and on the nightside the atmospheric density is dominated by O_2 up to altitudes of ~100 km and by H_2 there-above. In the following we will present an overview of previously published modeling efforts for Ganymede's atmosphere, focusing on the new aspects introduced by each model. A table listing the range of surface densities and column densities derived in each publication is given at the end of this Section in Table 2.

Marconi (2007) published the first 'classical' modeling attempt of Ganymede's atmosphere. The authors included sputtering and sublimation of H_2O, O_2, H_2, OH, O, and H in a collision-less to quasi-collisional 2D axisymmetric simulation. While calculations for the sublimation and sputter fluxes are presented, implemented source rates were in the end altered to match the available observations. The derived densities and column densities thus have to be taken with caution. Further collision-less models were published by Turc et al. (2014) and Plainaki et al. (2015). While Turc et al. (2014) added one dimension (making the model 3D) and photo-dissociative ionization as a loss mechanism, Plainaki et al. (2015) additionally included surface precipitation maps of three ion species (hydrogen, oxygen, and sulfur ions) at 5 energies (1, 5, 10, 50, and 100 keV) to simulate sputtering more accurately. Furthermore, Turc et al. (2014) investigated the effects that Ganymede passing into the shadow and found that the sublimated H_2O peak in the subsolar region disappears within one hour in the shadow of Jupiter. Plainaki et al. (2015), on the other hand, focus on the morphology of Ganymede's atmosphere, noticing sputter-induced leading/trailing and polar/equatorial H_2O atmosphere dichotomies and an O_2 atmosphere that comprises two regions (a near-surface thermal O_2 region that is associated with the thermalized O_2 molecules and an extended tenuous O_2 region that consists of more energetic O_2 molecules directly sputtered from the surface). The most recent collision-less model results were published by Vorburger et al. (2022), who implemented a 3D Monte-Carlo exosphere model of Ganymede's sublimated and sputtered H_2O atmosphere that focuses on the physics governing the release processes. In their simulation, they include precipitation maps of H^+, O^+, O^{++}, S^{+++}, and electrons with energies ranging from 10 eV to 100 MeV. Their model shows that H_2O sputtering is mainly induced by heavy ions, whereas protons and electrons contribute very little to the sputtered atmosphere.

Collisional modeling efforts of Ganymede's atmosphere were published by Shematovich (2016), Leblanc et al. (2017), and Leblanc et al. (2023). Shematovich (2016) shows that in the dense near-surface layer, collisions between H_2O and O_2 molecules among themselves but also with their supra-thermal photolysis and radiolysis products result in a substantial increase in the scale height of these species. Leblanc et al. (2017), on the other hand, concentrate on the temporal variability of Ganymede's atmosphere, and show that due to the seasonal variation there is a general atmospheric shift towards dusk, an O_2 'short term memory' (i.e., the O_2 exosphere at a given orbital position will depend on its history and evolution over about one Ganymede revolution), and a clear O_2 local dusk over local dawn asymmetry. Furthermore, Leblanc et al. (2023) analyze the orbital variability of Ganymede's atmosphere, showing that their model provides good agreement with observations obtained at four positions of Ganymede around its orbit (Roth et al., 2021; Leblanc et al., 2023; see also the discussion above).

One further set to mention here are the model results published in Carnielli et al. (2019, 2020b,a). Whereas in these models the atmosphere is not studied *per se*, the authors do investigate Ganymede's ionosphere using a 3D ionospheric model that includes the atmosphere simulation results published by Leblanc et al. (2017). The authors find that the derived electron density is consistently lower by at least an order of magnitude compared to observations, and that an O_2 atmosphere with a column density $>10^{\cdot 15}$ cm^{-2} is required to fit observations. Moreover, the authors compute new sputtering rates for Jovian ions, which are typically an order of magnitude higher compared to previous estimates, and investigate the role of ionospheric ions in sputtering, finding that these contribute at least 10% to the sputtering rates and under certain condition even dominate the sputter process.

In this work, we extend the work of Vorburger et al. (2022) with modeling results for O_2, H_2, O, and H. The release processes include sublimation, sputtering, and radiolysis. For sputtering and radiolysis, we use the same ion precipitation maps used in Vorburger et al. (2022), but we implement new precipitation maps (shown in Fig. 1) for electrons based on the recent Juno measurements (see Section 2.2). Since atomic O and H are produced mainly by the electron-dissociation of H_2O, O_2, and H_2, we show the column density produced for these species as a function of the electron environment (i.e., electron intensity) rather than presenting a single value.

2. Model description

2.1. Atmosphere Monte-Carlo model

Our Monte-Carlo model is a collision-less 3D test particle model that has been previously used to simulate the atmospheres of several Solar System bodies, including Callisto (Vorburger et al., 2015, 2019), Europa (Vorburger and Wurz, 2018; Vorburger and Wurz, 2021) and, most recently, Ganymede (Vorburger et al., 2022). In this paper, we model the atmospheres of the main species associated with Ganymede's water–ice surface (i.e., H_2O, O_2, H_2, O, and H). The validity of the assumption that Ganymede's atmosphere is non-collisional (except for the region near the subsolar point) has been shown previously to be generally valid (e.g., Marconi, 2007) and is not further investigated herein. Neutral molecules and atoms are ejected from the surface by either (i) sublimation (in the case of H_2O) or (ii) sputtering and radiolysis (in the case of all species investigated) and are traced on their elliptical or hyperbolic orbits under the influence of Ganymede's gravitational field until they are lost to either (i) gravitational escape, (ii) surface adsorption, (iii) ionization, or (iv) dissociation. Dissociation products are further traced until they either (i) escape, (ii) adsorb at the surface, (iii) are ionized, or, in the case of OH, (iv) are themselves dissociated. Detailed information on the implemented source and loss processes (especially the production rates and energy distributions) is given in the Appendix, while the implemented photon and electron reaction rates are presented in Table 3 (see also Section 2.2 for a discussion on the electron environment).

To correctly simulate any atmosphere, altitude steps smaller than the minimum occurring scale height must be implemented. In our simulations, the smallest theoretical scale height is the scale height of thermalized O_2 at Ganymede's nightside temperature of 80 K, which is equal to 14.56 km. Simultaneously, the simulation domain must be large enough to contain the trajectories of (close to) all particles. This is especially relevant for very light species (i.e., H and H_2) and dissociation products, particles which readily escape Ganymede's gravitational influence and thus have to be traced out to Ganymede's Hill radius (approximately 12 Ganymede radii or ~32,000 km). Because vastly different altitude steps and simulation domains are required for the different species, we decided to set up several simulation grids, each suitable for a different type of atmosphere. Table 4 lists for each implemented species the considered source process(es), the altitude step size (resolution), the upper boundary of the implemented simulation domain (maximum altitude), the longitude and latitude resolution (geographic resolution), and the number of particles initialized (note that dissociation products are a product of the simulation itself and thus no fixed number of particles was initialized). In the case of H_2O and O_2 it has been checked that the number of particles that leave the simulation domain but that would return within Ganymede's Hill sphere is negligible. As in our previously published simulation of Ganymede's atmosphere (Vorburger et al., 2022), the subsolar point coincides with the anti-Jovian sub-point (i.e., Ganymede is at local noon along its orbit and half of the trailing and half of the leading hemisphere are sunlit), and Ganymede is located near the center of the current sheet.

Table 2
Surface density and column density ranges derived from atmospheric models. Note that the release fluxes implemented by Marconi (2007), Turc et al. (2014), and Shematovich (2016) were adjusted to match observations.

Species	Density [cm^{-3}]	Column density [cm^{-2}]	References
H_2O (subsolar)	7e8	6e15	Marconi (2007)
	1e9		Turc et al. (2014)
	3e8–1e9		Plainaki et al. (2015)
	3e8		Shematovich (2016)
		1e14–1e16	Leblanc et al. (2017)
	4e9	2e16	Vorburger et al. (2022)
		few 1e15	Leblanc et al. (2023)
H_2O (polar)	2e4	2e11	Marconi (2007)
	9e3		Turc et al. (2014)
	1e4		Plainaki et al. (2015)
	4e3		Shematovich (2016)
	3e5		Leblanc et al. (2017)
	2e4	3e11	Vorburger et al. (2022)
O_2	3e5–3e8	2e12–6e14	Marconi (2007)
	(1–9)e7	1e15	Turc et al. (2014)
		4e13	Plainaki et al. (2015)
	1e7		Shematovich (2016)
	(3–9)e7	2e14–2e15	Leblanc et al. (2017)
		(3.6–4.3)e14	Leblanc et al. (2023)
H_2	5e5–8e6	(1–3)e14	Marconi (2007)
	(1–8)e5		Turc et al. (2014)
	5e4–2e5		Shematovich (2016)
	2e6	2e14–1e15	Leblanc et al. (2017)
OH	1e3–1e5	2e10–4e12	Marconi (2007)
	4e2–8e3		Turc et al. (2014)
	8e2–8e3		Shematovich (2016)
O	(3–4)e4	8e11–2e12	Marconi (2007)
	(1–3)e3		Turc et al. (2014)
	4e2–2e3		Shematovich (2016)
H	1e3–1e4	3e11–2e12	Marconi (2007)
	2e2–1e3	2e10	Turc et al. (2014)
	2e2–3e4		Shematovich (2016)
		(4–6)e10	Leblanc et al. (2017)

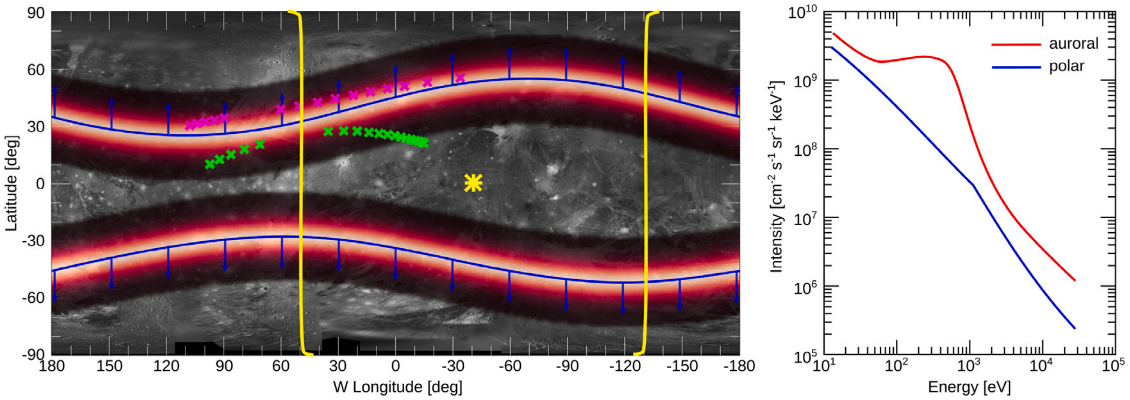

Fig. 1. Ganymede surface map (credit: Kersten et al., 2021) with the regions auroral and polar electrons have access to indicated in red and blue, respectively. Note that the auroral regions are implemented as a Gaussian distribution; here ±3 sigma are shown. The lightest color indicates maximum precipitation, whereas the darkest color indicates minimum precipitation within the ±3-sigma range. Over-plotted are Juno's sub-spacecraft points in green, Juno's magnetic field-line tracings in magenta, and the subsolar point as well as the terminators in yellow, as provided in Figure 5 of Greathouse et al. (2022). Also shown are the energy spectra for auroral and polar electrons (shown in red and blue, respectively) implemented according to Ebert et al. (2022). (For interpretation of the references to color in this figure legend, the reader is referred to the web version of this article.)

2.2. Plasma environment

Ions. In this study, ions are considered to interact with Ganymede's surface, but not with the atmosphere (i.e., neither atmospheric sputtering nor charge-exchange is included nor is possible energy deposition/attenuation of the plasma considered). Accordingly, for ions, only the flux that precipitates onto Ganymede's surface is relevant here. The ion precipitation fluxes used herein are the same fluxes that have already been applied to Ganymede's surface in Vorburger et al. (2022), where Ganymede's water exosphere resulting from sublimation, ion sputtering, and electron sputtering was studied in detail. The ion precipitation fluxes were obtained by coupling hybrid simulations (presented in Fatemi et al., 2016) with a test-particle model (presented in Poppe et al., 2018), and include thermal H^+ and O^+ and energetic H^+, O^{++}, and S^{+++}. Thermal ions cover the energy range 10 eV to 100 keV, whereas energetic ions cover the energy range 1 keV to 10 MeV. The total precipitation flux ranges from $7.28 \cdot 10^3$ m^{-2} s^{-1} to $8.88 \cdot 10^8$ m^{-2} s^{-1}, with a H^+:O^{n+}:S^{+++} ratio of ~4:15:1. For a more detailed description of the ion precipitation fluxes please refer to Section 2.2 and Figure 1 in Vorburger et al. (2022). While this composition of the ambient plasma near Ganymede is consistent with Voyager and Galileo measurements, we note that more-recent observations suggest

Table 3
Implemented reaction rates. Excess energies are only given for reactions producing neutral species and the same energies are assumed for electron impact reactions as those calculated by Huebner et al. (1992) for the analogous photo-chemical reactions. For electrons, there are two rates per interaction process. The first rate is for interactions with polar electrons, whereas the second rate is for interactions with auroral electrons. Note that in our simulation electron reactions with polar electrons can only occur in areas poleward of the OCFB, whereas reactions with auroral electrons can occur within a 15° FWHM wide band centered around the OCFB.

Reaction		Electron population	Rate [s^{-1}]	Excess energy [eV]	Reference
$H_2O + h\nu$	$\rightarrow OH + H$	–	3.81e−7	3.41	Huebner et al. (1992)
$H_2O + h\nu$	$\rightarrow O + H + H$	–	2.79e−8	0.70	Huebner et al. (1992)
$H_2O + h\nu$	$\rightarrow H_2 + O$	–	2.21e−8	3.84	Huebner et al. (1992)
$H_2O + h\nu$	$\rightarrow H_2O^+ + e^-$	–	1.22e−8		Huebner et al. (1992)
$O_2 + h\nu$	$\rightarrow O + O$	–	1.50e−7	1.43	Huebner et al. (1992)
$O_2 + h\nu$	$\rightarrow O_2^+ + e^-$	–	1.73e−8		Huebner et al. (1992)
$H_2 + h\nu$	$\rightarrow H + H$	–	3.40e−9	5.00	Huebner et al. (1992)
$H_2 + h\nu$	$\rightarrow H_2^+ + e^-$	–	2.00e−9		Huebner et al. (1992)
$OH + h\nu$	$\rightarrow O + H$	–	7.34e−7	4.36	Huebner et al. (1992)
$OH + h\nu$	$\rightarrow OH^+ + e^-$	–	8.99e−9		Huebner et al. (1992)
$O + h\nu$	$\rightarrow O^+ + e^-$	–	9.13e−9		Huebner et al. (1992)
$H + h\nu$	$\rightarrow H^+ + e^-$	–	2.68e−9		Huebner et al. (1992)
$H_2O + e^-$	$\rightarrow OH + H$	polar	2.63e−7	3.41	Itikawa and Mason (2005), Ebert et al. (2022)
$H_2O + e^-$	$\rightarrow H_2 + O$	polar	2.76e−8	3.84	Ip (1997), Carnielli et al. (2019)
$H_2O + e^-$	$\rightarrow H_2O^+ + e^-$	polar	2.89e−7		Itikawa and Mason (2005), Ebert et al. (2022)
$O_2 + e^-$	$\rightarrow O + O$	polar	7.96e−8	1.43	McConkey et al. (2008), Ebert et al. (2022)
$O_2 + e^-$	$\rightarrow O_2^+ + e^-$	polar	3.23e−7		McConkey et al. (2008), Ebert et al. (2022)
$H_2 + e^-$	$\rightarrow H + H$	polar	1.76e−7	5.00	Scarlett et al. (2018), Ebert et al. (2022)
$H_2 + e^-$	$\rightarrow H_2^+ + e^-$	polar	1.27e−7		Straub et al. (1996), Ebert et al. (2022)
$OH + e^-$	$\rightarrow O + H$	polar	5.07e−7	4.36	Ip (1997), Carnielli et al. (2019)
$OH + e^-$	$\rightarrow OH^+ + e^-$	polar	2.76e−7		Joshipura et al. (2017), Ebert et al. (2022)
$O + e^-$	$\rightarrow O^+ + e^-$	polar	2.01e−7		Thompson et al. (1995), Ebert et al. (2022)
$H + e^-$	$\rightarrow H^+ + e^-$	polar	1.76e−7		Deutsch et al. (2014), Ebert et al. (2022)
$H_2O + e^-$	$\rightarrow OH + H$	auroral	1.98e−6	3.41	Itikawa and Mason (2005), Ebert et al. (2022)
$H_2O + e^-$	$\rightarrow H_2 + O$	auroral	2.76e−8	3.84	Ip (1997), Carnielli et al. (2019)
$H_2O + e^-$	$\rightarrow H_2O^+ + e^-$	auroral	2.59e−6		Itikawa and Mason (2005), Ebert et al. (2022)
$O_2 + e^-$	$\rightarrow O + O$	auroral	5.65e−7	1.43	McConkey et al. (2008), Ebert et al. (2022)
$O_2 + e^-$	$\rightarrow O_2^+ + e^-$	auroral	3.10e−6		McConkey et al. (2008), Ebert et al. (2022)
$H_2 + e^-$	$\rightarrow H + H$	auroral	8.20e−7	5.00	Scarlett et al. (2018), Ebert et al. (2022)
$H_2 + e^-$	$\rightarrow H_2^+ + e^-$	auroral	9.75e−7		Straub et al. (1996), Ebert et al. (2022)
$OH + e^-$	$\rightarrow O + H$	auroral	5.07e−7	4.36	Ip (1997), Carnielli et al. (2019)
$OH + e^-$	$\rightarrow OH^+ + e^-$	auroral	2.30e−6		Joshipura et al. (2017), Ebert et al. (2022)
$O + e^-$	$\rightarrow O^+ + e^-$	auroral	1.78e−6		Thompson et al. (1995), Ebert et al. (2022)
$H + e^-$	$\rightarrow H^+ + e^-$	auroral	1.00e−6		Deutsch et al. (2014), Ebert et al. (2022)

Table 4
Simulation setups. Note that for dissociation products no value is given for the number of particles initialized, since they are a direct product of the simulation itself.

Species	Source process	Altitude resolution	Maximum altitude	Geographic resolution	Number of particles
H_2O	sublimation	5 km	1,200 km	1°×1°	2e6
	sputtering	35 km	32,000 km	2°×2°	2e6
O_2	radiolysis	5 km	4,800 km	2°×2°	2e6
H_2	radiolysis	75 km	32,000 km	2°×2°	2e6
	dissociation of H_2O	75 km	32,000 km	2°×2°	–
OH	sputtering	50 km	32,000 km	2°×2°	2e6
	dissociation of H_2O	200 km	32,000 km	2°×2°	–
O	sputtering	50 km	32,000 km	2°×2°	2e6
	dissociation of H_2O, O_2 and OH	200 km	32,000 km	2°×2°	–
H	sputtering	50 km	32,000 km	2°×2°	2e6
	dissociation of H_2O, H_2, and OH	200 km	32,000 km	2°×2°	–

additional ion charge states that we have not considered here (see, e.g., Allen et al., 2019; Clark et al., 2020; Kim et al., 2020). Since the dynamics of ions with like composition but with an additional charge are similar (e.g., the gyroradii of S^{+++} which is included within the model compared to S^{++} which is not remain within a factor of 2), we expect that including additional charge states would not strongly alter our results. However, we note that a rigorous investigation of the effect of differently charged ions near Ganymede is beyond the scope of this study.

NASA's Juno spacecraft encountered a close flyby of Ganymede in 2021 with the closest approach of 1,046 km. During the flyby, Ganymede was located close to the Jovian plasma sheet (approximately (−2)° magnetic latitude during the closest approach; see e.g., Saur et al., 2022) with the lower limit of observed ambient electron density of ~ 4 cm^{-3} (Allegrini et al., 2022). Although the geometry of the flyby was markedly different compared to the previous Galileo flybys of Ganymede, the Jovian plasma environment of Ganymede was similar to that of the Galileo's G8 flyby, also simulated by Fatemi et al. (2016) and Poppe et al. (2018). Therefore, the plasma precipitation patterns obtained from the aforementioned modeling studies are applicable to generate neutral atmosphere through surface sputtering during the Juno flyby of Ganymede.

Electrons. Liuzzo et al. (2020) and Vorburger et al. (2022) studied electrons from 4.5 keV to 100 MeV. However, the electron energies that are most relevant for particle sputtering and interactions with atmospheric particles are in the eV – 10 s of keV range (Teolis et al., 2017; Galli et al., 2018). Recently JADE characterized the electron environment near Ganymede in this energy range, thus presenting new information on the electron environment most relevant for this work (Allegrini et al., 2022). The measurements were taken on 7 June 2021, as Juno passed within 1046 km of Ganymede's surface during its 34th perijove (Hansen et al., 2022). During this flyby, Juno approached Ganymede from the South, passed through a part of the wake region, through its magnetosphere to closest approach on the nightside, to the dayside, and back into the plasma disk towards Jupiter. For more information on Juno's trajectory, please refer to Hansen et al. (2022), in particular their Figure 2 and Table 2.

As already discussed in Section 1.1, auroral observations have shown that Ganymede's magnetosphere strongly influences the electron environment, with electron acceleration into Ganymede's auroral bands (see e.g., McGrath et al., 2013 and Eviatar et al., 2001). We accordingly considered two electron populations in this paper: The polar electrons, which are assumed to reach surface regions poleward of the open-closed field line boundary (OCFB), and the auroral electrons, which are assumed to reach Ganymede's auroral bands. In our model, the auroral bands are described by a Gaussian distribution centered around the OCFB (implemented according to Duling et al., 2022), with a full width at half maximum of 15°. Equator-ward of the OCFB, electrons at the considered energies cannot penetrate the closed field line region, and therefore are unable to directly access the surface (Liuzzo et al., 2020).

Due to the lack of measurements at lower altitudes, we made some simplifying assumptions in this work. The most critical assumption is that the differential fluxes measured at Juno's altitude can be extrapolated to Ganymede's surface and that they are, depending on Juno's location, representative of either the polar electrons or the auroral electrons on the surface of Ganymede. Consequences of this assumption are discussed in Section 3. For the polar electrons we used the electron differential flux measured by JADE in Jupiter's plasma sheet (Figure 3 in Ebert et al., 2022). For the auroral electrons, we used the differential flux measured by JADE at Ganymede's magnetopause current layer (also Figure 3 in Ebert et al., 2022). Within JADE's energy range ($\sim$10 eV to few keV), these electrons exhibit an average partial density of ~ 7 cm^{-3}. These measurements were not actually taken within the flux tubes connected to the auroral bands, as Juno does not appear to have crossed the OCFBs (see also the magenta symbols in Fig. 1 denoting Juno's magnetic field-line tracings in magenta). However, Ebert et al. (2022) state that the electrons denoted by the red curve in their Figure 3 (see also Fig. 1 herein) show field-aligned intensity enhancements to the highest energies observed within this transit of Ganymede's magnetopause current layer and that they correspond to a time when the magnetic field observations indicate the presence of magnetic flux ropes. Furthermore, they conclude with "These observations place constraints on the energies that electrons can be accelerated to during this process [magnetic reconnection], electron distributions that may reflect those that are responsible for producing Ganymede's aurora". (Ebert et al., 2022). For more information on the auroral and magnetospheric observations conducted by Juno please refer to Greathouse et al. (2022), Allegrini et al. (2022), Clark et al. (2022), Romanelli et al. (2022) and Kurth et al. (2022).

Fig. 1 shows the regions where the auroral (red) and polar (blue) electrons are assumed to have access to. Also shown in Fig. 1, in the same colors, are approximations of the auroral and polar energy spectra (Ebert et al., 2022). Note that contrary to ions, electrons are considered to interact both with the surface (through sputtering and radiolysis) and with the atmosphere (through ionization and dissociation). For the latter, we assume that the electron reaction rates are constant with altitude.

It is noteworthy that a fraction of the Juno-measured electrons can reflect back into space as they move closer to Ganymede due to the increase in the parallel component of Ganymede's magnetic field ($\nabla_{\parallel} B \neq 0$). If we assume that the spatial and temporal variations of Ganymede's magnetic fields are small over either a gyro-orbit or a gyro-period of an electron, as a first order approximation we can apply conservation of the first adiabatic invariant into the motion of precipitating electrons over the polar and auroral regions (i.e., $d\mu/dt = 0$, where μ is the magnetic moment) (see Roederer and Zhang, 2014 for a discussion on the applicability of the first adiabatic invariant under given conditions). Therefore, we can assume the energy of an electron remains constant along an equipotential magnetic field line, and hence,

$$\frac{sin^2(\alpha(s))}{B(s)} = \frac{sin^2(\alpha_0)}{B_0} = const., \tag{1}$$

where α is the pitch angle, s is the length of a magnetic field line arc, and α_0 as well as B_0 are the initial particle's pitch angle and magnetic field at an arbitrary point, respectively. Since the electron intensity in our calculations has been taken from Juno's observations during the outbound magnetopause crossing of Ganymede (Hansen et al., 2022), α_0 and B_0 are the pitch angle and magnetic field intensity at the magnetopause. Considering conservation of the first adiabatic invariant (Eq. (1)), for an electron to impact the surface of Ganymede, its pitch angle at the magnetopause should follow

$$sin^2(\alpha_{\rm mp}) \le \frac{B_{\rm mp}}{B_{\rm surf}}, \tag{2}$$

where $\alpha_{\rm mp}$ is the pitch angle at the magnetopause, $B_{\rm mp}$ and $B_{\rm surf}$ are the intensity of the magnetic fields at the magnetopause and on the surface of Ganymede, respectively. During the Juno flyby of Ganymede, $B_{\rm mp} \simeq 100$ nT (Allegrini et al., 2022) and the surface magnetic field strength at the open-closed field line boundaries ($\sim$60° latitude) $B_{\rm surf} \simeq 1100$ nT. Applying these values into Eq. (2), all electrons with pitch angle smaller than 17° at the magnetopause impact the surface of Ganymede. Juno observations of Ganymede have shown that around half of the down-going electrons at the magnetopause have pitch angles smaller than 17° (Allegrini et al., 2022). This indicates that only about half of the electron intensity measured at Juno reach the surface of Ganymede, a fact we account for in our model.

We furthermore note that the brightness of Ganymede's auroral ovals significantly vary in longitude (Marzok et al., 2022) and over time (Saur et al., 2022) and may be non-continuous and patchy. How representative the single JADE measurement outside the OCFB is, is difficult to assess at this point. In lack of more information, our used map assumes that this electron flux represents the average auroral electron precipitation.

2.3. Ganymede surface properties

For Ganymede's surface temperature field we use the same assumptions as applied in Vorburger et al. (2022): The surface temperature ranges from 80 K to 150 K, with the dayside temperature connected to the constant nightside temperature by a $\cos^{3/4}$-function. Please refer to Section 2.3.2 and Figure 1 of Vorburger et al. (2022) for more details on the implemented surface temperature field.

As in Vorburger et al. (2022), we implement a variable water–ice concentration for Ganymede's surface based on the ice concentration maps presented by Ligier et al. (2019). The water–ice concentration is in the range ~8%–58%, with values in the polar regions being generally higher than values in the equatorial regions. As Ganymede is constantly bombarded by energetic particles (effectively radiation), Ganymede's water–ice does not consist of 100% of H_2O molecules. Indeed, observations have shown that on Ganymede the intense charged particle environment has produced O_2, H_2O_2, and O_3 in the icy surface (Spencer et al., 1995; Noll et al., 1996). As radiolysis turns H_2O into H_2 and 1/2 O_2, H_2 should also be produced in the ice but has yet to be observed. One caveat is that the actual H_2 content at a given time inside the ice will be lower than 2 times the O_2 content because it cannot be effectively retained inside the ice (Bar-Nun et al., 1985; Galli et al., 2018) compared to O_2 (Grieves and Orlando, 2005; Loeffler et al., 2006; Zheng et al., 2006; Galli et al., 2018). O, H, and OH are too reactive to exist in a stable form at Ganymede's surface temperature range. We collected data from spectroscopic observations of Ganymede's surface ice and from laboratory ice irradiation experiments to determine an ice composition that is representative of Ganymede's surface ice. The derived composition for Ganymede's water–ice (the surface concentration of which ranges from ~8% to 58%, as mentioned above) consists to 96.5% of H_2O molecules, 2% of H_2 molecules, 1% of O_2 molecules, 0.5% of H_2O_2 molecules, and 0.001% of O_3 molecules (with only the first three species being considered in this study). In the case of sputtering, new surface ice species can be created as the impinging ions and electrons interact with the surface (i.e., as a neutral particle is released it can simultaneously be dissociated). These modifications are represented in the sputter yields that are presented in the Appendix.

3. Results & discussion

Since the different species in Ganymede's atmosphere exhibit vastly different characteristics, we present our results for each species separately in the following.

3.1. H_2O

The H_2O atmosphere can be divided into two populations: the sublimated H_2O atmosphere and the sputtered H_2O atmosphere. As already shown in Vorburger et al. (2022), the sublimated H_2O atmosphere dominates the sputtered H_2O atmosphere in the subsolar region by several orders of magnitude. The sublimated H_2O atmosphere is highly variable, though, decreasing quickly with increasing solar zenith angle and/or increasing altitude (see, e.g., Figure 4 in Vorburger et al. (2022)). The top left panel of Fig. 2 accordingly shows three different density profiles for the sublimated H_2O atmosphere: The maximum sublimated atmosphere in the subsolar region (i.e., within 5 degrees of the subsolar point), the average sublimated atmosphere on the dayside (i.e., within 90 degrees of the subsolar point), and the average global sublimated atmosphere. For sputtering, which produces a spatially much less variable atmosphere than sublimation, a different subdivision was made, i.e., one by source agent. Fig. 2 accordingly shows three curves for sputtering as well: One for sputtering by ions, one for sputtering by polar electrons, and one for sputtering by auroral electrons.

As mentioned in Appendix A.1.1, the electron sputter yield is not well known for H_2O. At 500 eV, the only energy at which a H_2O electron sputter yield was measured in the laboratory, the electron sputter yield is ~3 times lower than the H^+ sputter yield, about 50 times smaller than the O^+ sputter yield, and ~100 times smaller than the S^+ sputter yield. Overall, the H_2O production rate due to electron sputtering is approximately 20 times lower than due to ion sputtering.

As mentioned above, for electrons, two different populations were investigated. Polar electrons have access to a larger surface area than auroral electrons do, but the intensity of auroral electrons is higher than the intensity of polar electrons (especially at higher energies due to electron acceleration in the auroral region, see Fig. 1). Our simulations show that auroral electrons provide 2.5 times more H_2O than polar electrons do.

The top central panel in Fig. 2 shows the line-of-sight (LOS) column density taken from a point located far from Ganymede (e.g., Earth) and looking at the sunlit hemisphere (note that the subsolar point is in the center of the disk). This panel provides the most applicable data product for comparison with Earth-based spectroscopic observations of Ganymede's atmosphere (e.g., images taken by the HST). The variability of the sublimated atmosphere (mainly on the disk) is also shown here to contrast strongly with the uniformity of the sputtered atmosphere, which dominates the off-disk regions. As it is not easy to read absolute values from a color-plot, we also show cross-sections through the column density plot, running from north to south through the subsolar point (panel to the right) and from west to east along the equator (bottom panel). In these cross-sections, the division into the sublimated atmosphere (within ±1 Ganymede radius) and the sputtered atmosphere is also very clear.

Note, that neither in Fig. 2 nor in the following model result figures error-bars are plotted. Instead, we provide an analytic error-estimation here. The main error sources of our modeling efforts are introduced by input uncertainties and variations. For each species, the dominant modeling input parameters are (i) the precipitation flux, (ii) the surface concentration, (iii) the surface temperature, and (iv) the sputter yield (see also Appendix). Based on literature, we estimate that the precipitation flux is known to about one order of magnitude (see, e.g., Kivelson et al., 2004), the surface concentration uncertainties are on the order of a few percent (see, e.g., Ligier et al., 2019), surface temperatures uncertainties are also on the order of a few percent (see, e.g., Spencer, 1987; Orton et al., 1996), and the sputter yields are known to about a factor of 2. Except for temperature, which exponentially influences the H_2O vapor pressure in case of sublimation, all other errors propagate linearly.

Table 5 provides a more detailed analysis of the contributions of the various release processes. In the first column, the total release of H_2O molecules from Ganymede's surface is listed. As one can see, sublimation releases more than three orders of magnitude more H_2O molecules into the atmosphere than sputtering does. Columns two through four present different column densities: the resulting mean global (dayside and nightside) column density, the resulting mean dayside only column density, and the resulting maximum column density.

The maximum H_2O column density inferred from observations is equal to $> 4.8 \cdot 10^{15}$ cm^{-2} (Roth et al., 2021). This value agrees well with our maximum sublimated column density of $\sim 2 \cdot 10^{16}$ cm^{-2}, but is much higher than the maximum sputtered column density of $\sim 4 \cdot 10^{12}$ cm^{-2}. The (Roth et al., 2021) observations of Ganymede's H_2O atmosphere are thus clearly dominated by sublimated H_2O, with the sputtered atmospheric H_2O signal being too faint to be distinguishable from the sublimated H_2O signal. Nevertheless, sputtering is not a negligible process for Ganymede's H_2O atmosphere, as it is mainly sputtering that populates higher altitudes in Ganymede's atmosphere, the region a spacecraft (and, consequently, *in situ* measurements) have access to, as has already been discussed in Section 4 of Vorburger et al. (2022).

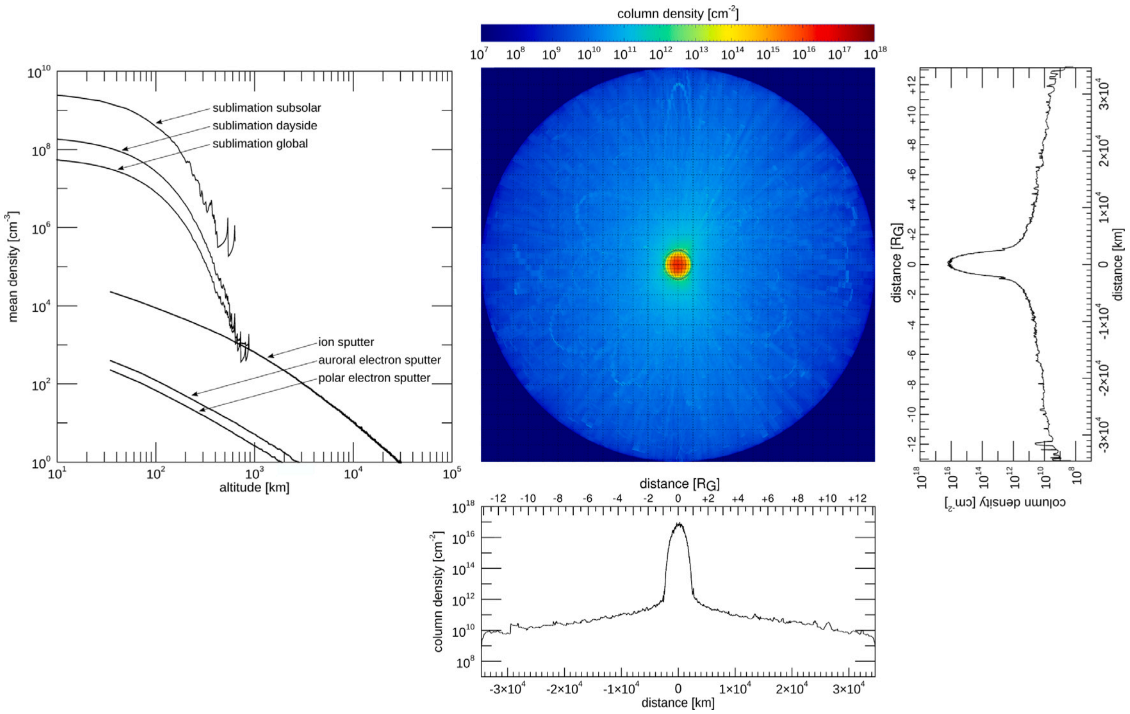

Fig. 2. Model results for H_2O released by both sublimation and sputtering. The central plot shows the column density integrated along the LOS. The left plot shows radial H_2O density profiles for sublimation and sputtering separately versus altitude above the surface. For sublimation, three curves are shown: The maximum sublimated atmosphere in the subsolar region (i.e., within 5 degrees of the subsolar point), the dayside (i.e., sunlit hemisphere) sublimated atmosphere, and the global sublimated atmosphere (i,e, including the nightside). For sputtering, the contributions by the three inducing sources are shown: H_2O sputtered by ions, H_2O sputtered by auroral electrons, and H_2O sputtered by polar electrons. The panels to the right and the bottom show the LOS column density (i.e., 'into the page' column density) running from north to south through the subsolar point (panel to the right) and from west to east along the equator (bottom panel).

Table 5
H_2O modeled global release rate (rel), mean global (dayside and nightside) column density ($<NC_{global}>$), mean dayside column density ($<NC_{dayside}>$), and maximum column density (max(NC)) for each release process considered as well as the maximum column density inferred from observations (Roth et al., 2021).

Process	Release [s^{-1}]	$<NC_{global}>$ [cm^{-2}]	$<NC_{dayside}>$ [cm^{-2}]	Max(NC) [cm^{-2}]
H_2O sublimation	9.11e29	3.47e14	6.91e14	1.76e16
H_2O ion sputter	6.43e26	6.13e11	7.06e11	3.67e12
H_2O polar electron sputter	8.11e24	4.43e09	4.58e09	1.66e10
H_2O auroral electron sputter	2.04e25	7.81e09	8.31e09	7.35e10
H_2O inferred from observation	–	–	–	**> 4.8e15**

3.2. O_2

The atmospheric density profile of O_2 differs significantly from the density profile of H_2O. This is mainly due to the non-condensing nature of O_2 in the temperature range of Ganymede's surface temperature. After an initial 'hop', the non-condensing O_2 molecules keep 'bouncing' off the surface, being re-emitted at the local surface temperature whenever they interact with the surface. This 'bouncing' leads to an enhanced near-surface atmosphere, as the molecules keep accumulating in the low-altitude region until they are removed either through ionization or through dissociation (with virtually no molecules lost to escape or adsorption). The O_2 atmosphere thus comprises two populations, the O_2 molecules initially released by radiolysis, which exhibit lower densities but larger scale heights, and the thermalized O_2 molecules, which exhibit larger densities but smaller scale heights.

In the top left panel of Fig. 3, the dashed, gray lines show the density profiles of the radiolytically produced O_2 molecules, whereas the solid, gray lines show the final atmospheric density profiles, with the difference showing the effect of the O_2 accumulation in the near-surface (first few hundred km) atmosphere. Again, three different curves are shown, one for O_2 radiolysis initiated by ions, one for O_2 radiolysis initiated by polar electrons, and one for O_2 radiolysis initiated by auroral electrons. The sum of all contributions (ion radiolysis, polar electron radiolysis, and auroral electron radiolysis) is shown by the solid, black line. According to laboratory measurements, the ratio between the ion and the electron sputter yield is not as high for O_2 as it is for H_2O (e.g., Teolis et al., 2017). In fact, at low energies, the ion and electron sputtering yields are remarkably similar, and the sputtering yields begin to differ noticeably only at higher energies.

The LOS column density of the dayside O_2 atmosphere is shown in the top central panel of Fig. 3. Note that, contrary to H_2O, the O_2 column density distribution is very similar on the dayside, the nightside, the sub-Jovian, and the anti-Jovian hemisphere in our 'snapshot' simulation (i.e., ignoring long-term effects), with only minor differences due to the local surface temperatures (and thus scale heights). As already shown in the density plot, the LOS column density is highly increased on and close to the disk due to the enhanced near-surface atmosphere with thermalized O_2. The top right and bottom panels show two cross-sections through the top middle panel, taken from north to south through the subsolar point and from west to east along the equator. On the disk, the LOS column density integral is limited from the boundary of the simulation domain to the disk. Off the disk, the LOS column density integral is not spatially limited, ranging in theory from minus infinity to plus infinity. This abrupt transition from a limited to an unlimited integral can be seen by the enhanced peaks in the column density plots at ±1 Ganymede radius. Off the disk,

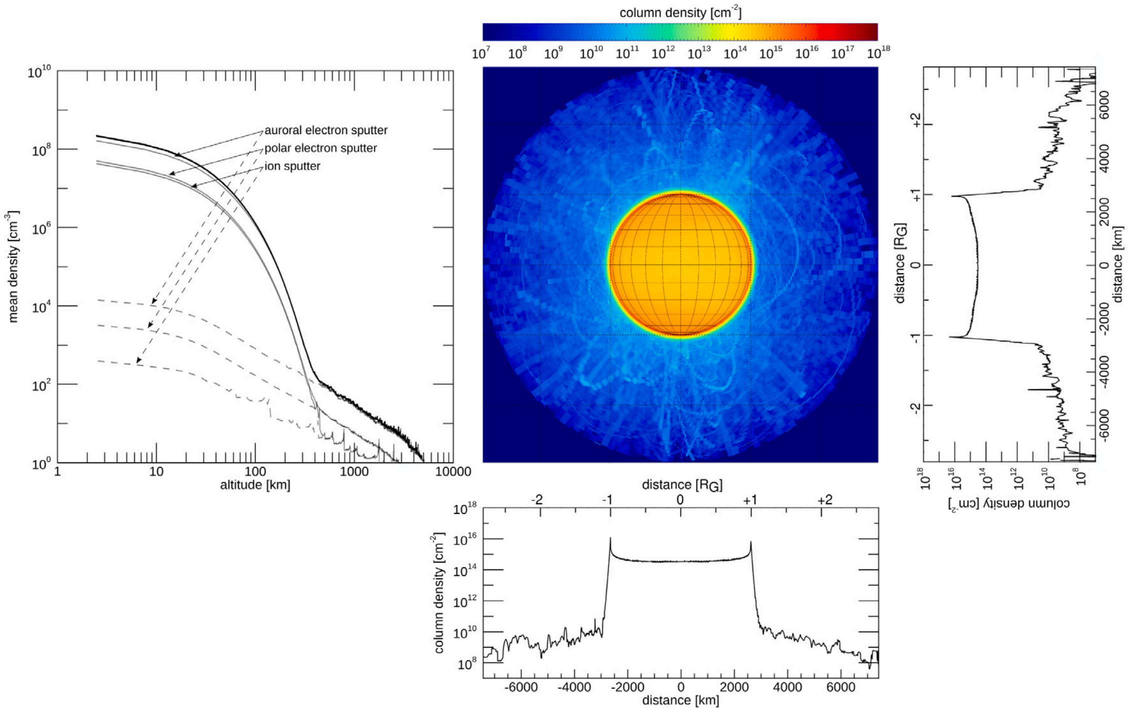

Fig. 3. Model results for O_2 released by radiolysis. The central plot shows the column density integrated along the LOS (the subsolar point is in the center of the image). The left plot shows the average total radial density profile (solid, black line) versus altitude above the surface. Over-plotted in dashed, gray lines are the particles that have been initially released and in solid, gray lines the final density profiles of the three radiolysis contributions. The difference between the dashed lines and the solid lines shows the effect of thermalization of the non-condensing gas. The panels to the right and the bottom show the LOS column density (i.e., 'into the page' column density) running from north to south through the subsolar point (panel to the right) and from west to east along the equator (bottom panel).

the column density drops abruptly, transitioning from the enhanced near-surface atmosphere to the column density profile of the initially released molecules.

Table 6 presents the O_2 release rates and resulting column densities for each process considered in detail. The similarity of the values in columns two through four of this table highlights the uniform nature of Ganymede's O_2 atmosphere (in contrast to the non-uniform nature of Ganymede's H_2O atmosphere; see Table 5). As discussed above, when 'bouncing', non-condensing molecules are only destroyed through ionization and dissociation. As such, the atmospheric density keeps increasing in the near-surface region until the lifetime of the molecules balances their loss rates. As mentioned in Section 2 and shown in Table 3, the loss rates are reaction-specific. In addition, for each reaction, molecules can only be lost if they are within a region where the reaction partner (i.e., photon or electron) is present, i.e., on the sunlit hemisphere for reactions with photons, in the polar region for reactions with polar electrons, and in the auroral regions for reactions with auroral electrons. Our simulations have shown that the lifetimes of the O_2 molecules allow for about 1e4 bounces (corresponding to $\sim 10^6$ s), which is mainly limited through the reaction with auroral electrons, which produces loss rates larger by a factor of ~5 and ~10 than the loss rates due to reactions with polar electrons and photons, respectively.

Comparison of our modeled atmospheric O_2 column densities to O_2 column densities inferred from observations shows that our results agree well with observations (see Table 6): We derive an O_2 column densities of $4.44 \cdot 10^{14}$ cm^{-2}, which is right in the range of the observationally inferred O_2 column densities ($3 \cdot 10^{13}$–$1 \cdot 10^{15}$ cm^{-2}).

3.3. H_2

Just like O_2, H_2 is a non-condensing gas at the thermal conditions of Ganymede and therefore behaves similarly to the O_2 gas, forming a global thermal H2 atmosphere. However, as can be seen in Fig. 4, the H_2 densities are quite different from the O_2 densities. Most notably, the H_2 density profiles do not show a distinct transition from a radiolytically produced population to thermally accommodated population. The main differences in magnitude and shape of the H_2 and the O_2 density curves result from the different molecular masses of the two species. With H_2 molecules being so light, a significant fraction of molecules can escape even after the initial 'hop', which is not the case for O_2 molecules. While H_2 thus accumulates in the atmosphere like O_2, the increase over the initially released molecules is about 10 times lower for H_2 than for O_2 (i.e., ~1000 instead of ~10,000), due to the H_2 molecules being lost to space in addition to being lost to ionization and dissociation, even after the initial 'hop'. In addition, the shape of the final density profiles resembles the shape of the density profiles of the initially released particles. Fig. 4 shows in the top left panel the final total density profile in solid, black, the density profiles of the initially released H_2 molecules in dashed, gray, and the final density profiles of the individual contributions in solid, gray. Since the H_2 radiolysis release process is very similar to the O_2 radiolysis release process (though the H_2 sputter yields are higher by a factor of 2 due to stoichiometric reasons), the relative contributions of the three radiolysis processes (ion radiolysis, polar electron radiolysis, and auroral electron radiolysis) are equal for O_2 and H_2.

The central panel in Fig. 4 shows the LOS column density of the H_2 atmosphere. Also here, the atmosphere is densest close to the surface. However, the decrease with altitude is much shallower than for O_2, due to the much larger scale height of H_2, resulting in densities being still quite high at high altitudes. As previously, we show the cross sections through the 2D LOS column density in the top, right and the bottom panels. In these panels the gradual decrease with altitude is also well evident.

No neutral H_2 has yet been observed in Ganymede's atmosphere (ionized H_2, on the other hand, has recently been observed (see Szalay et al., 2022), but we expect H_2 to be present due to stoichiometric reasons (see Appendix). In Table 7, we present the release rates and the

Table 6
O_2 modeled global release rate (rel), mean global (dayside and nightside) column density ($<NC_{global}>$), mean dayside column density ($<NC_{dayside}>$), and maximum column density (max(NC)) for each release process considered as well as the maximum column density inferred from observations (see Table 1).

Process	Release [s^{-1}]	$<NC_{global}>$ [cm^{-2}]	$<NC_{dayside}>$ [cm^{-2}]	Max(NC) [cm^{-2}]
O_2 ion radiolysis	4.65e25	7.62e13	6.68e13	2.08e14
O_2 polar electron radiolysis	5.36e25	9.88e13	8.53e13	2.28e14
O_2 auroral electron radiolysis	2.38e26	3.25e14	3.10e14	6.33e14
O_2 inferred from observation	–	–	**3e13–1e15**	–

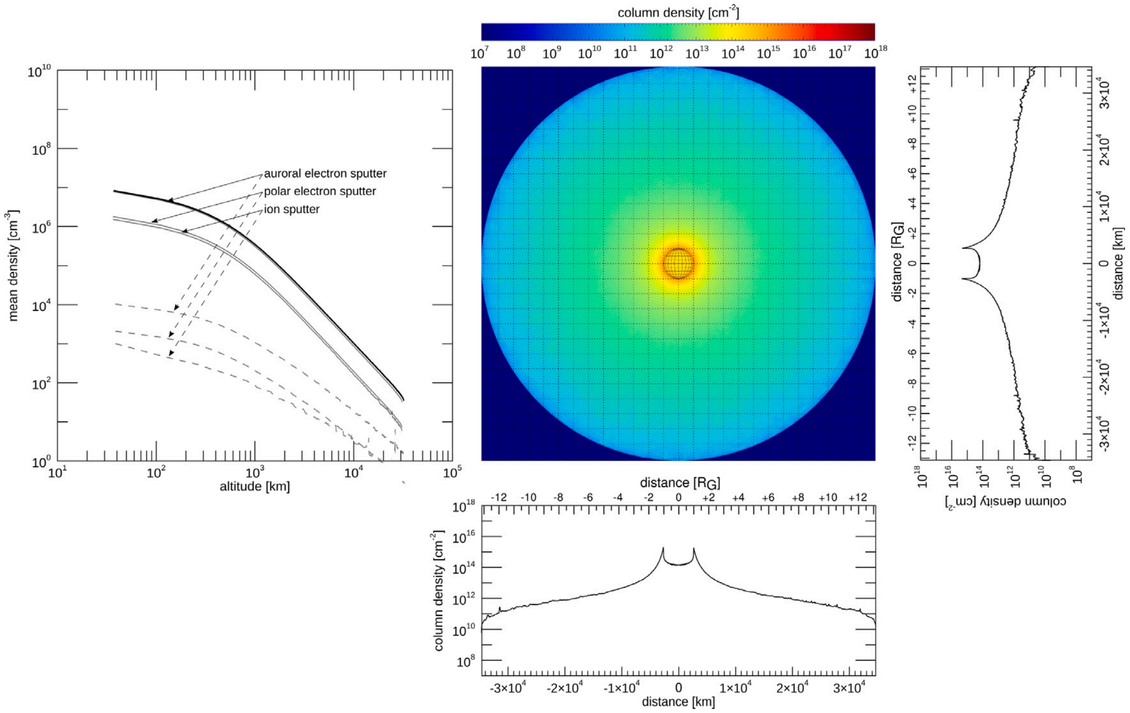

Fig. 4. Model results for H_2 released by radiolysis. The central plot shows the column density integrated along the LOS (the subsolar point is in the center of the image). The left plot shows the average radial density profiles (solid lines) versus altitude above the surface. Over-plotted by dashed lines are the particles that have been initially released by the radiolysis processes. The difference between the dashed lines and the solid lines show the effect of thermalization of the non-condensing gas. The plots to the right and the bottom show the LOS column density taken along the equator (bottom) and along the axis connecting the north and the south pole (right).

Table 7
H_2 modeled global release rate (rel), mean global radial column density ($<NC_{global}>$), mean dayside radial column density ($<NC_{dayside}>$), and maximum radial column density (max(NC)) for each release process considered. No observational constraints for H_2 exist to date.

Process	Release [s^{-1}]	$<NC_{global}>$ [cm^{-2}]	$<NC_{dayside}>$ [cm^{-2}]	Max(NC) [cm^{-2}]
H_2 ion radiolysis	9.30e25	4.35e13	3.15e13	8.61e13
H_2 polar electron radiolysis	1.07e26	4.93e13	3.60e13	7.34e13
H_2 auroral electron radiolysis	4.75e26	2.12e14	1.55e14	3.23e14

column densities of each radiolysis source. The H_2 release rates are, due to stoichiometric reasons, twice the O_2 release rates. However, the LOS column densities of H_2 only amounts to about 60% of the LOS column density of O_2 due to the lower accumulation factor mentioned above. Our model shows that auroral electrons dominate the sputter contribution to Ganymede’s H_2 atmosphere, while polar electrons and ions yield similar H_2 densities. Again, as it was the case for O_2, columns two through four are quite similar for H_2, highlighting the uniform global nature of the H_2 atmosphere. While no observationally inferred column-densities are available, we compare our model results to previous model results of other groups. The range of previously published H_2 column densities (see Table 2) is equal to $1{\cdot}10^{14}$–$1{\cdot}10^{15}$ cm^{-2} and agrees very well with our results, which are on the order of a few 10^{14} cm^{-2}.

3.4. O

Table 8 lists the total global source rates of O (and H) atoms, broken down by source mechanisms. The same photon and electron environment described in Section 2.2 and the reaction rates given in Table 3 were used for dissociation. For direct sputtering the same ion and electron precipitation fluxes were used as for the molecular species discussed above. Table 8 shows that the main sources of atomic O in Ganymede’s atmosphere are the dissociation of O_2 molecules released by radiolysis and the dissociation of sublimated H_2O molecules. Directly sputtered O results in approximately 100 times lower global source rates than dissociation does.

Since dissociation is the main source process for O in Ganymede’s atmosphere, the amount of O added per second is highly dependent on the electron and photon environment. Ganymede’s charged particle environment is highly variable, though, both in space and time. We thus determine the O column densities as a function of reaction rate for each source process. Such an analysis allows one to determine for any possible photon and electron environment the resulting O column density. The resulting analysis is shown in Fig. 5, where we present the average global O column density as a function of reaction rate for three different parent molecules (sublimated H_2O [solid lines], sputtered H_2O

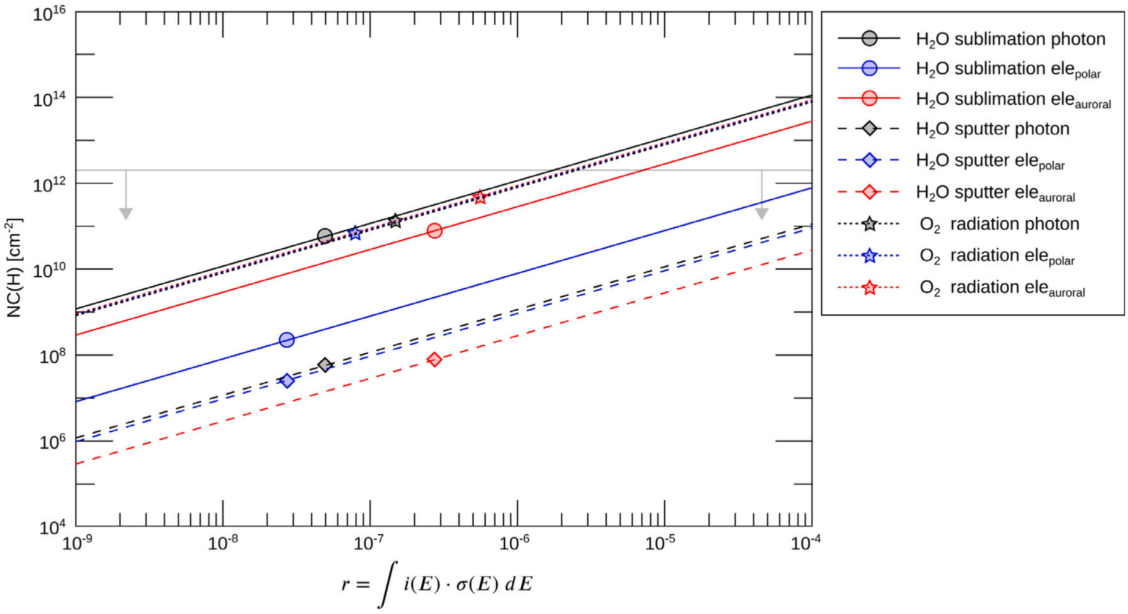

Fig. 5. O column densities resulting from nine different source processes: sublimated H_2O dissociated by photons (black solid line), sublimated H_2O dissociated by polar electrons (blue solid line), sublimated H_2O dissociated by auroral electrons (red solid line), sputtered H_2O dissociated by photons (black dashed line), sputtered H_2O dissociated by polar electrons (blue dashed line), sputtered H_2O dissociated by auroral electrons (red dashed line), O_2 released by radiolysis and dissociated by photons (black dotted line), O_2 released by radiolysis and dissociated by polar electrons (blue dotted line), and O_2 released by radiolysis and dissociated by auroral electrons (red dashed line). The curves show the relationship between the O column density and the reaction rate of the respective process, whereas the symbol denotes our current best estimate of the specific reaction processes. Also shown in gray is the current best estimate of the O column density based on observational constraints ($<2 \cdot 10^{12}$ cm^{-2}, Roth et al., 2021). (For interpretation of the references to color in this figure legend, the reader is referred to the web version of this article.)

Table 8
Global O and H source rates.

Source process	O Source rate [s^{-1}]	H Source rate [s^{-1}]
dissociation of sublimated H_2O	6.07e25	4.95e26
dissociation of sputtered H_2O	1.37e23	1.01e24
dissociation of sputtered OH	2.44e22	2.44e22
dissociation of radiolyzed O_2	1.54e26	–
dissociation of radiolyzed H_2	–	3.95e26
direct sputtering of O	1.47e24	–
direct sputtering of H	–	2.94e23
total	2.16e26	8.91e26

[dashed lines], and O_2 released by radiolysis [dotted lines]) and three different reactions (dissociation by photons [black], dissociation by polar electrons [blue], and dissociation by auroral electrons [red]). In the plot, the lines denote for each source process the correlation between the O column density and the reaction rate, whereas the symbols give the column density resulting from the reaction rate presented in Table 3. Note that the offset in the *y*-direction between the different lines has two different reasons. First, the abundance of the underlying parent molecule is different for sublimated H_2O, sputtered H_2O, and sputtered O_2 (i.e., the number of molecules available for dissociation varies from species to species). Second, the region where the reaction partner (i.e., photon or electron) has access to is different for photons, polar electrons, and auroral electrons (i.e., the chance of a reaction partner to encounter a molecule which it can dissociate is different from case to case). The shift in *y*-direction is equal to the product of these two factors. In the following, we will discuss each line and symbol in detail.

Photons can dissociate both sublimated and sputtered H_2O. Fig. 5 shows that for the same reaction rate, photons reacting with sublimated H_2O (solid black line) produce almost three orders of magnitude higher O column densities than photons reacting with sputtered H_2O (dashed black line) do. Based on Huebner et al. (1992), the current best estimate for the photon-dissociation rate of H_2O at Ganymede's distance is equal to $5.0 \cdot 10^{-8}$ s^{-1}, resulting in O column densities of $5.87 \cdot 10^{10}$ cm^{-2} and $6.20 \cdot 10^{7}$ cm^{-2} for sublimated and sputtered H_2O, respectively. Polar electrons also produce more O atoms when interacting with sublimated H_2O (solid blue line) than with sputtered H_2O (dashed blue line). Here, the ratio between the O column densities associated with the two source processes is less than 10, though. Our computed reaction rate for polar electrons and H_2O molecules is $2.76 \cdot 10^{-8}$ s^{-1}, resulting in O column densities of $2.28 \cdot 10^{8}$ cm^{-2} and $2.61 \cdot 10^{7}$ cm^{-2} for sublimated and sputtered H_2O, respectively. Finally, a third way of dissociating H_2O molecules in Ganymede's atmosphere is through interactions with auroral electrons. Here, again, the O column densities produced through the interaction with sublimated H_2O (solid red line) is almost three orders of magnitude higher than the O column densities produced through the interaction with sputtered H_2O (dashed red line). Our computed reaction rate for H_2O molecules and auroral electrons is $\sim 2.76 \cdot 10^{-7}$ s^{-1}, resulting in column densities of $7.74 \cdot 10^{10}$ cm^{-2} and $8.30 \cdot 10^{7}$ cm^{-2} for sublimated and sputtered H_2O, respectively.

Please note, that these values present a 'snapshot' of the interaction between Ganymede's H_2O atmosphere and Ganymede's electron environment. In the modeled configuration, Ganymede is at local noon along its orbit, where half of the trailing and half of the leading hemisphere are sunlit. According to Musacchio et al. (2017), the auroral oval is shifted 4.1° towards Ganymede's planetographic equator on the leading hemisphere and 2.9° towards the poles on the trailing hemisphere. The reaction rates between H_2O molecules and electrons is thus maximized when the leading hemisphere is fully illuminated, as in that configuration the electrons can reach lower latitudes where more sublimated H_2O molecules are present. We calculate that the reaction rates between the minimum configuration (when the trailing hemisphere is illuminated) and the maximum configuration (when the leading hemisphere is illuminated) vary by about a factor of 7, with the configuration presented herein representing an intermediate configuration.

The reaction between photons, polar electrons, and auroral electrons with O_2 molecules is less complicated than with H_2O. In the case of O_2, molecules keep accumulating in the atmosphere until a balance between the source and the loss rate is established. As such, the production of atomic O from O_2 is limited by this balance, and the correlation between O column density and reaction rate is the same for photons, polar electrons, and auroral electrons (i.e., the three dotted lines are identical). What is different, though, are the values of the current best estimates for the reaction rates for the three interactions (see Table 3). The reaction rate is smallest for polar electrons interacting with O_2 ($\sim 7.96 \cdot 10^{-8}$ s^{-1}), highest for auroral electrons interacting with O_2 ($\sim 5.65 \cdot 10^{-7}$ s^{-1}), and intermediate for photons interacting with O_2 ($\sim 1.5 \cdot 10^{-7}$ s^{-1}). The resulting O column densities are $6.94 \cdot 10^{10}$ cm^{-2} (polar electrons), $4.92 \cdot 10^{11}$ cm^{-2} (auroral electrons), and $1.31 \cdot 10^{11}$ cm^{-2} (photons), respectively.

Finally, the gray horizontal line in Fig. 5 shows the upper boundary for the O column density inferred from observations (Roth et al., 2021). The derived upper boundary ($2 \cdot 10^{12}$ cm^{-2}) agrees well with our results, being approximately 4 times higher than the maximum column density we derive ($4.92 \cdot 10^{11}$ cm^{-2}; auroral electrons dissociating O_2) when applying the reaction rates presented in Table 3. From all the previous model efforts, only Marconi (2007) presents O column density in their paper. The authors (who scale their source fluxes to match observations) derive O column densities ranging from $8 \cdot 10^{11}$ cm^{-2} to $2 \cdot 10^{12}$ cm^{-2}. These values are compatible with the highest value we derive ($\sim 5 \cdot 10^{11}$ cm^{-2}), though they are somewhat higher.

Since in our simulations dissociation is modeled by creating two new particles that travel in opposing directions, as a rule of thumb, about half the O source rate presented in Table 8 is lost to escape. The reasoning behind this is that about half of the created particles travel on a downward trajectory, being lost to surface adsorption as they encounter Ganymede's surface, whereas the other half travels upward, being lost to escape. Numerical simulation outputs confirm this rule of thumb.

3.5. H

Similar to atomic oxygen, atomic hydrogen in Ganymede's atmosphere is mainly the product of dissociation of H_2O and H_2 (see Table 8). As such, similar aspects apply for the overall column density of H as for O: Whereas we can determine the H column density based on our current best knowledge of the reaction rates, the actual H column density in Ganymede's atmosphere is strongly dependent on the local photon and electron environments, which is highly variable. We accordingly present a H column density plot similar to the O column density plot in Fig. 6, where for any given H_2O and H_2 source process and rate the resulting H column density can be read out.

Photons can dissociate sublimated H_2O as well as sputtered H_2O. The ratio between the resulting H column densities is ~340:1, with more H being produced through the photon-dissociation of sublimated H_2O (black solid line) than through the photon-dissociation of sputtered H_2O (black dashed line). Our current best estimate for the reaction rate between photons and H_2O that produce atomic H at Ganymede is $\sim 4.37 \cdot 10^{-7}$ s^{-1}, resulting in column densities of $9.56 \cdot 10^{9}$ cm^{-2} and $2.82 \cdot 10^{7}$ cm^{-2} for sublimated and sputtered H_2O, respectively. The ratio between H column density for polar electrons interacting with sublimated (blue solid line) and sputtered H_2O (blue dashed line) is only about 20, i.e., much less than the photon-related ratio. Our current best estimate for the H-producing reaction rate between polar electrons and H_2O molecules in Ganymede's atmosphere is $\sim 2.63 \cdot 10^{-7}$ s^{-1}, yielding H column densities of $2.72 \cdot 10^{8}$ cm^{-2} and $1.42 \cdot 10^{7}$ cm^{-2} for dissociation of sublimated and sputtered H_2O, respectively. Similarly to photons, auroral electrons interacting with sublimated H_2O (red solid line) result in H column densities approximately 550 times higher than auroral electrons interacting with sputtered H_2O (red dashed line). The H-producing reaction rate between auroral electrons and H_2O in Ganymede's atmosphere is approximately $1.98 \cdot 10^{-6}$ s^{-1}, resulting in H column densities of $1.79 \cdot 10^{10}$ cm^{-2} and $3.25 \cdot 10^{7}$ cm^{-2} for sublimated and sputtered H_2O, respectively.

As mentioned in the subsection above, the interaction between photons and electrons with non-condensing gases is much simpler than with condensing gases. Here, a balance between production and loss rate is established, so that the H column density is limited by this balance. This results in equal H column densities for photons, polar electrons, and auroral electrons interacting with H_2. However, our current best estimate of the reaction rates between photons, polar electrons, and auroral electrons and H_2 yield vastly different rates and, consequently, resulting column densities. The latter range from $4.59 \cdot 10^{8}$ cm^{-2} for photons reacting with H_2 to $1.34 \cdot 10^{10}$ cm^{-2} for polar electrons reacting with H_2 to $1.07 \cdot 10^{11}$ cm^{-2} for auroral electrons dissociating H_2.

Comparison to the current best range of H column densities inferred from observations ($(1.5–2.2) \cdot 10^{12}$ cm^{-2}) shows that the H column densities we derive are lower by about one order of magnitude. The reason for this discrepancy might be that (i) different electron environments were assumed (see Fig. 6), (ii) the H densities derived from observations are overestimated for unknown reasons, or (iii) because we under-estimate the underlying H_2O or H_2 column density (the main source of H in Ganymede's atmosphere). Underestimation of H_2O seems unlikely, as our results agree well with observations, and are, in fact, rather on the upper limit of the observations. Underestimation of H_2 is difficult to assess, because no observational constraints for the H_2 abundance in Ganymede's atmosphere were ever reported. If we consider stoichiometric considerations, though, and the fact that our O_2 results agree well with observations, it seems plausible that also our H_2 abundances are not too far off. If, however, we indeed underestimate the abundance of H_2 in Ganymede's atmosphere, then an additional feature not considered here could become important: intermolecular collisions. At Callisto, Carberry Mogan et al. (2022) showed that although the morphology of H is similar to that of its parent species (H_2O, H_2) – regardless if collisions in the atmosphere are considered or not – collisions between the hot H (produced via the same mechanisms considered here) and the thermal atmospheric components, in particular the extended H_2, can enhance the H density by as much as an order of magnitude (depending on the density of H_2) as the latter thermalizes the former. If this is also applicable here, this would explain the discrepancies between our results and the observations.

Finally, comparing our derived global H column density ($\sim 1 \cdot 10^{11}$ cm^{-2}) to previously modeled H column densities shows that we agree well with previous modeling works. Turc et al. (2014), for example, derives typical H column densities of $\sim 2 \cdot 10^{10}$ cm^{-2}, whereas Leblanc et al. (2017) derives maximum H column densities of $\sim 6 \cdot 10^{10}$ cm^{-2}. Both results are similar to the results we derive, and one to two orders of magnitude lower than observations. Marconi (2007) is the only model that provides H column densities agreeing with the observations ($3 \cdot 10^{11}–2 \cdot 10^{12}$ cm^{-2}). However, one must keep in mind that Marconi (2007) scaled their source fluxes to match the available observations.

Similar to the oxygen atoms, it is about half the H release rate mentioned in Table 8 that is lost to escape for dissociated sublimated H_2O. For sputtering, where the parent molecules travel much faster and thus usually reach much higher altitudes before they are dissociated, this value is even higher (~70%–80%), as at these high creation altitudes even particles traveling 'downwards' might 'miss' Ganymede's surface and escape. Thus, for H atoms, as a rule of thumb, about half of the atoms originating in sublimated parent molecules escape, whereas about 70% to 80% of H atoms originating in sputtered parent molecules escape.

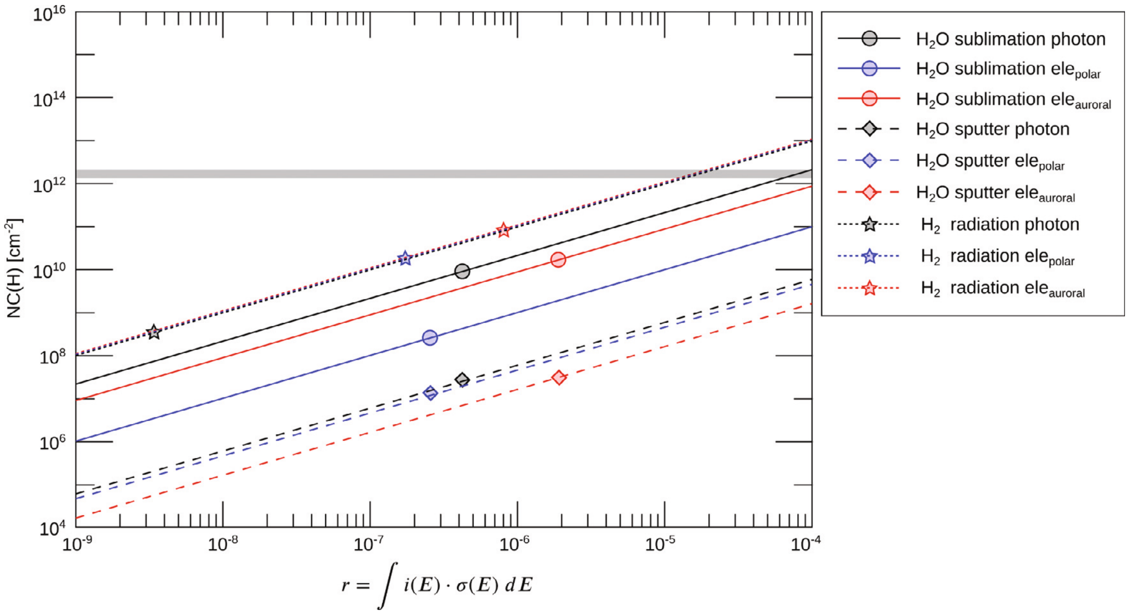

Fig. 6. H column densities resulting from nine different source processes: sublimated H_2O dissociated by photons (black solid line), sublimated H_2O dissociated by polar electrons (blue solid line), sublimated H_2O dissociated by auroral electrons (red solid line), sputtered H_2O dissociated by photons (black dashed line), sputtered H_2O dissociated by polar electrons (blue dashed line), sputtered H_2O dissociated by auroral electrons (red dashed line), H_2 released by radiolysis and dissociated by photons (black dotted line), H_2 released by radiolysis and dissociated by polar electrons (blue dotted line), and H_2 released by radiolysis and dissociated by auroral electrons (red dashed line). The curves show the relationship between the H column density and the reaction rate of the respective process, whereas the symbol denotes our current best estimate of the specific reaction processes. Also shown in gray is the current best estimate of the H column density range determined from observational constraints ($(1.5\text{–}2.2)\cdot 10^{12}$ cm^{-2}). (For interpretation of the references to color in this figure legend, the reader is referred to the web version of this article.)

4. Conclusion

We present ab-initio modeling results of Ganymede's atmosphere. These modeling results present a generalized picture of Ganymede's atmosphere, giving a global overview of the atmospheric density, composition, and morphology. In reality, Ganymede's atmosphere is not only highly complex but also highly variable, and dependent on a wide variety of parameters. In our model we have accounted for all major processes that are involved in the creation and loss of Ganymede's atmosphere. To characterize the ongoing processes, we have implemented observationally inferred parameters (e.g., surface temperatures, electron intensities, ion fluxes, sputter yields). These parameters stem from different observations and measurements, though, (e.g., from the Galileo mission, the Juno mission, laboratory experiments). They are also neither free of ambiguities nor uncertainties, and are in addition valid only for a specific location and time. What would be required for a holistic understanding of Ganymede's atmosphere are simultaneous observations of Ganymede's surface, atmosphere, and plasma environment taken at different times and locations. Simultaneous *in situ* measurements of Ganymede's atmosphere, electron, and ion environment (preferably together with magnetic field data) would provide deep insights into the physical and chemical processes governing Ganymede's atmosphere.

Despite all uncertainties and unknowns, over the past 15 years a consistent picture of Ganymede's atmosphere has emerged: Close to the subsolar point, the atmosphere is dominated by sublimated H_2O, while the non-condensing gases O_2 and H_2 make up most of the atmosphere at higher solar zenith angles and at higher altitudes. Ion- and electron-sputtering also delivers H_2O to the atmosphere, but while the scale height of the sputtered H_2O molecules is much higher, their density is much lower than that of the sublimated H_2O. Nevertheless, H_2O sputtering is also an important process in Ganymede's atmosphere, because it is sputtering that delivers H_2O molecules to high altitudes where they can be measured *in situ* by a spacecraft. The O_2 and H_2 atmosphere, in contrast, is primarily produced as a result of ion and electron irradiation, being radiolytically created within the ice before it diffuses out. Due to its non-condensing nature, O_2 and H_2 keeps accumulating in the near-surface atmosphere, until a balance between the source and the loss flux is reached.

Our simulations suggest for the first time that Ganymede's O_2 and H_2 atmosphere is primarily controlled by the electron environment: According to our simulations, electrons are not only mainly responsible for the surface release of O_2 and H_2 (see Tables 6 and 7) but also for their destruction (i.e., ionization and dissociation). The electron environment in Ganymede's vicinity, in turn, is strongly influenced by Ganymede's magnetic field. In the closed field-line region (i.e., in the equatorial region), Ganymede's surface is shielded from precipitating low-energy electrons, leaving it only exposed to high-energy electrons. While high-energy electrons can induce radiolysis, followed by the diffusion of O_2 and H_2, at higher energies (> tens of keV) the electrons penetrate to depths where most radiolysis products remain trapped and therefore the release of O_2 and H_2 decreases. In the open field-line region (i.e., in the polar region), electrons can freely precipitate onto Ganymede's surface to efficiently liberate O_2 and H_2. Finally, in the separatrix (i.e., the region of the open closed field line boundary), electrons are accelerated towards the surface by the electro-magnetic environment (see, e.g., Eviatar et al., 2001). One of the open questions we addressed in this paper is how much auroral electrons and polar electrons contribute to Ganymede's atmosphere in comparison to ions.

Thanks to the very recent Juno Ganymede flyby, new energy spectra have become available for Ganymede's electron environment. We have included these spectra in our Monte-Carlo model, parametrizing their surface access to the best of our knowledge (see Fig. 1). The measurements by Juno were made at an altitude of >1046 km and in other regions than those considered in our study, yet these measurements provide the currently best constraints on Ganymede's electron environment. Tables 6 and 7 as well as Figs. 3 and 4 show that the auroral electrons, as inferred from the Juno observations, are the main agent responsible for delivering O_2 and H_2 into Ganymede's atmosphere. Simultaneously, our simulations show that it is the auroral electrons that limit the lifetime of the non-condensible gases, thus determining by how much these gases can accumulate in the near-surface environment before they are removed from the atmosphere.

To validate our assumption of utilizing the electrons observed by Juno as auroral electrons, we conducted an assessment of the oxygen emission brightness that our derived O_2 atmosphere, in conjunction with the implemented electron spectrum, would yield. By integrating across the energy spectrum and employing emission cross-sections documented in the work of McConkey et al. (2008), we computed an OI 1356 Å emission brightness of approximately 20 Rayleighs. Feldman et al. (2000), Musacchio et al. (2017), and Molyneux et al. (2018) indicate that OI 1355 Å emissions within Ganymede's auroral region can reach levels as high as 300 Rayleighs. At first glance, this discrepancy may suggest that our implemented electron spectrum falls short by a factor of roughly 10 to 15. However, it is important to recognize that augmenting the electron density has a dual impact on emission brightness: (i) an increase in electrons directly translates to more emissions, and (ii) a higher electron count correlates with elevated O_2 densities (as our analysis reveals that auroral electrons serve as the primary source of O_2 in Ganymede's atmosphere, see Table 6). Assuming O_2 scales linearly with the electron flux, and aurora brightness scales linearly with both O_2 abundance and electron flux, 3–4 times higher electron flux was needed to yield 10–15 times brighter aurora as observed. If indeed the electron flux was higher, this would only support our main conclusion that electron sputtering is the main source for O_2 and H_2, while for H_2O sublimation is still the clearly dominant source.

Since the auroral electrons are mainly responsible for the removal of O_2 and H_2 from the atmosphere through ionization and dissociation, they are also mainly responsible for the addition of atomic O and H to Ganymede's atmosphere. For these two atomic species the local electron properties are thus especially relevant. As mentioned above, though, the electron environment is highly variable, both in space and time. Thus no set of parameters can be thought of as being representative on a global scale. We therefore decided to conduct an analysis that shows the atomic O and H column abundance as a function of reaction rate. In the future, once measurements of Ganymede's electron and photon environments become available, these plots can be used to read out the resulting O and H column density for any determined reaction rate.

Previous modeling efforts have failed to re-create the high atomic O and H abundances that have been inferred from spectroscopic observation by up to two orders of magnitude (see e.g., Turc et al., 2014 and Leblanc et al. (2017) for a discussion on this matter). Our modeling efforts show that including an auroral electron environment helps in this matter. Our derived O column density of $\sim 5 \cdot 10^{11}$ cm^{-2} agrees well with the observationally inferred upper boundary of $2 \cdot 10^{12}$ cm^{-2}. Our derived H column density of $1 \cdot 10^{11}$ cm^{-2} is still an order of magnitude short of the observationally inferred H column density of $(1.5\text{–}2.2) \cdot 10^{12}$ cm^{-2}. As mentioned in the very beginning, to infer atmospheric column densities from spectroscopically observed line emission brightnesses, assumptions about the emission inducing electron environment have to be made. If these assumptions are off, e.g., by either assuming wrong electron and photon intensities or energy spectra, this will directly result in an error in the inferred atmospheric column density. Furthermore, as H is mainly added to Ganymede's atmosphere through dissociation, it is possible that we either under-estimated the underlying parent molecule abundance or the dissociation reaction rates thereof. If the former is the case, intermolecular collisions could enhance the H density by an order of magnitude, removing the discrepancy between our results and the available observations. Finally, as previously mentioned, the atmosphere and electron environment are not only spatially but also temporally highly variable. It is thus possible that both the observations and the model results are correct, and that they just show different snapshots of the atmosphere in time.

In summary, the most important findings made in this paper are:

- H_2O is mainly added to Ganymede's atmosphere through sublimation. With a maximum surface temperature of 150 K, a maximum radial column density of $\sim 2 \cdot 10^{16}$ cm^{-2} is achieved, agreeing well with the maximum H_2O column density derived from observations, which is equal to $> 4.8 \cdot 10^{15}$ cm^{-2} (Roth et al., 2021).
- Comparing the low energy (eV to keV) to the high energy (keV to MeV) electrons, low energy electron sputtering delivers about 50 times more H_2O molecules to the atmosphere than high energy electrons do (see Vorburger et al., 2022).
- O_2 and H_2 are mainly added to the atmosphere through radiolysis, with auroral electrons dominating the source flux. At the same time, it is the auroral electrons that are mainly responsible for removing O_2 and H_2 from Ganymede's atmosphere (i.e., through impact ionization and impact dissociation). For these two non-condensing molecules, electrons thus mainly govern how much O_2 and H_2 can accumulate in the atmosphere.
- We derive average dayside radial O_2 column densities of $\sim 4.6 \cdot 10^{14}$ cm^{-2}, a value that agrees well with the range of column densities inferred from observations ($(3 \cdot 10^{13}\text{–}1 \cdot 10^{15})$ cm^{-2}). Our derived H_2 column density is $\sim 2.2 \cdot 10^{14}$ cm^{-2}, about half the column density of O_2. Whereas according to stoichiometric considerations, in Ganymede's surface, the amount of available hydrogen is twice the amount of available oxygen, hydrogen is much lighter than oxygen and thus much more prone to escape.
- Atomic O and H are mainly added to Ganymede's atmosphere through the dissociation of molecular O_2 and H_2 already in the atmosphere. As the amount of O and H added strongly depends on the electron environment, we compiled Figs. 5 and 6 showing the relationship between the O and H column density and the electron environment.
- To compare our derived O and H column densities to observations, we determined the O and H column densities corresponding to the electron properties that were inferred from Juno's Ganymede flyby. The derived O column density of $5 \cdot 10^{11}$ cm^{-2} agrees well with the observationally inferred upper boundary of $2 \cdot 10^{12}$ cm^{-2}. The derived H column density of $1 \cdot 10^{11}$ cm^{-2} is one order of magnitude lower than the observationally inferred range of $(1.5\text{–}2.2) \cdot 10^{12}$ cm^{-2}.
- As a rule of thumb, about half of the O source rates and about 50% to 80% of the H source rates mentioned in Table 8 are lost to escape, depending on the source mechanism.

The work presented herein shows how strongly Ganymede's atmospheric properties depend on a multitude of endogenic and exogenic parameters. The same is true for the interpretations of available observations: To correctly infer atmospheric densities from line emissions, a good understanding of the electron environment is crucial. In this study, we have presented new model results for Ganymede's atmosphere, where we have incorporated current best estimates for the parameters describing the governing processes. Based on these simulations we have determined the relative importance of competing processes. One has to keep in mind, though, that the values used herein represent best efforts, and that these parameters are not only uncertain but also highly variable, both spatially and temporally.

To get a full understanding of Ganymede's atmosphere it is thus crucial that the ion environment, the electron environment, and the neutral atmosphere are measured simultaneously *in situ*, an endeavor which the Particle Environment Package (PEP) onboard JUICE will undertake. PEP combines a neutral gas mass spectrometer, electron spectrometers, ion spectrometers, and energetic neutral atom imagers, measuring particles at all relevant energies (Barabash et al., 2016; Galli et al., 2022). The current JUICE trajectory foresees 12 flybys at Ganymede (closest approaches between 400 km and 66,000 km) before JUICE will enter into orbit around Ganymede. This orbit will first be an elliptical orbit with an apocenter of ~10,000 km and a pericentre of ∼200 km, that evolves into a circular near-polar orbit in its final phase at 500 km altitude. This way, PEP will sample Ganymede's atmosphere and the space environment for diverse combinations of solar illumination, geographic latitude, open vs. closed field lines, and Ganymede position with respect to the Jovian magnetosphere, providing us with a holistic picture of Ganymede's atmosphere. Moreover, near-simultaneous PEP and JUICE's Ultraviolet Spectrograph (UVS) measurements will provide validation of the assumptions and methods used to interpret remote observations of Ganymede's aurora, allowing more accurate long-term monitoring of the atmosphere even after the JUICE mission ends.

Declaration of competing interest

The authors declare that they have no known competing financial interests or personal relationships that could have appeared to influence the work reported in this paper.

Data availability

Data will be made available on request.

Acknowledgments

A. V., A. G., and P. W. acknowledge support from the Swiss National Science Foundation, Switzerland (SNSF) grant 200020_207409. A. V. and S. F. acknowledge support from the Swedish National Space Agency, Sweden (SNSA), grant 179/18. S.F. also acknowledges support from the Swedish Research Council, Sweden (VR), grant 2018-03454. We also acknowledge the fruitful discussions with J. W. Hunter and the JADE team on the JADE measurements.

Appendix

A.1. Model implementation

A.1.1. Sources

As source processes we consider (i) sublimation and (ii) sputtering and radiolysis, the dominating release processes on Ganymede (see e.g., Galli et al., 2023). In addition, O and H particles can be created through the dissociation of parent molecules. For each source process and each species of interest we need to know the particles' (i) production rates (or source flux) and (ii) energy distributions. In the following three paragraphs we will present implementation details on all three source processes as they pertain to H_2O, O_2, H_2, O, and H.

Sublimation. In our model, we assume that only H_2O is subject to sublimation. The H_2O sublimation flux is given by:

$$J_{H_2O} = \frac{p_{H_2O}}{k_B T}\sqrt{\frac{8 k_B T}{\pi m_{H_2O}}}, \tag{3}$$

where p_{H_2O} is the water vapor pressure (given, e.g., by equations 5 and 6 in Fray and Schmitt, 2009), k_B is the Boltzmann constant, T is the local surface temperature, and where m_{H_2O} is the molecular mass of H_2O. For each surface location, this flux has to be multiplied with the water's local surface concentration (see Section 2.3). The energy distribution for sublimating H_2O molecules is described by a Maxwell–Boltzmann distribution:

$$f_{H_2O}(E)dE = 2\sqrt{\frac{E}{\pi}}\left(\frac{1}{k_B T}\right)^{3/2}\exp\left(\frac{-E}{k_B T}\right)dE, \tag{4}$$

where k_B the Boltzmann constant and T is the local surface temperature (80–150 K).

Sputtering and radiolysis. When ions and electrons impact Ganymede's icy surface, direct or indirect particle release can be induced as a result. In the following, we refer to the direct release of H_2O, O, and H as sputtering, whereas we refer to the production and loss of H_2 and O_2 as radiolysis (see discussion above). The flux of sputtered and radiolytically produced molecules and atoms is equal to the flux of precipitating particles (ions or electrons) multiplied with the efficiency of the interaction, i.e., the sputter yield:

$$J_i = \int J_j(E)\cdot Y_{i,j}(E)dE, \tag{5}$$

where $J_j(E)$ is the precipitation flux of species j (i.e., H^+, O^+, O^{++}, S^{+++}, or electrons) at energy E and $Y_{i,j}(E)$ is the sputter or radiolysis yield of species i (i.e., H_2O, O_2, H_2, O, and H) due to the impingement of species j at energy E. The sputter yield ($Y_{i,j}(E)$) is not only a function of (i) the mass of the species released, (ii) the mass of the impinging particle, and (iii) the energy of the impinging particle, but also of (v) the angle of incidence, and (vi) the temperature of the surface. For the H_2O ion sputter yield, we implemented Equation 3 in Famá et al. (2008) and Figure 1 of Cassidy et al. (2010). For the O_2 and H_2 ion radiolysis yields we use Equations 11 and 12 in Teolis et al. (2017), respectively. In ion sputtering experiments, no directly released H, O, or OH has been observed to date. For these species, accordingly, only upper limits on the sputter yields have so far been determined. For the present work, we analyzed laboratory measurements to derive the following sputter yield constraints, which we used herein: $H/H_2 < 0.01$, $O/O_2 < 0.1$, and $OH/H_2O < 0.1$. Electron sputter experiments have so far mainly produced sputter yield curves for the release of O_2. In our simulation we use the O_2 and H_2 electron radiolysis yields presented (as for ions) in Equations 11 and 12 in Teolis et al. (2017) together with the results presented in Figure 5 of Galli et al. (2018), assuming that the yield remains constant at energies >0.5 keV.

Electron sputter yields for H_2O are still under investigation. Whereas Galli et al. (2017) measured only little H_2O relative to H_2 and O_2 being directly ejected by impinging electrons, Davis et al. (2021) infer from the y-intercept of their total mass loss curve a H_2O sputter yield of 0.17. While this value was determined for water–ice temperatures ranging from 14.5 K to 124.5 K, and for an electron energy of 0.5 keV, we use this value as the constant H_2O electron sputter yield for the complete temperature- and energy-range in lack of more data available.

In the following, the energy distribution first of sputtered H_2O, then of sputtered OH, O, and H, and finally of O_2 and H_2 released by radiolysis is presented. For sputtering of H_2O, the incoming particle's mass and energy determines if the particle release occurs in the nuclear or the electronic sputtering regime. For nuclear sputtering of H_2O, we use the energy distribution function given by Sigmund (1981):

$$f(E)dE = \frac{2UE}{(U+E)^3}\left[1-\left(\frac{U+E}{E_i}\right)^{1/2}\right]dE, \tag{6}$$

where U is the surface binding energy (0.055 eV for H_2O according to Reimann et al., 1984) and E_i is the energy of the incident particle. For electronic sputtering of H_2O, we assume a thermal energy distribution:

$$f(E)dE = 2\sqrt{\frac{E}{\pi}}\left(\frac{1}{k_B T}\right)^{3/2}\exp\left(\frac{-E}{k_B T}\right)dE, \tag{7}$$

but with an additional E^{-2} tail (added numerically and not shown in the equation above), which was observed in laboratory ice sputtering experiments (see e.g. Johnson and Liu, 1996; Johnson et al., 2002, 2013). Since OH, O, and H are highly reactive, we assume that these species are only released by nuclear sputtering processes. For these species, we use the same surface binding energy as for H_2O, as have other modelers done previously (e.g., Marconi, 2007; Turc et al., 2014; Leblanc et al., 2017). In the case of radiolysis of O_2 and H_2, most particles leave the surface with a thermal distribution (agreeing with the fact that part of the released O_2 and H_2 particles are created via radiolysis within the ice before they diffuse out at the local surface temperature). But, as for electronic sputtering, also here an E^{-2} was observed in laboratory experiments (e.g., Johnson et al., 2009). We thus use for radiolysis of O_2 and H_2 the same energy distribution as for electronic sputtering.

Dissociation. Dissociation of molecules adds atoms to the simulation and is thus also considered a source process. In our simulations, dissociation is implemented stochastically, i.e., occurs as a discrete event determined by the reaction-specific dissociation rate (see Table 3). When a dissociation event along the particle's trajectory occurs, two new particles are created, both of which receive, in addition to the current velocity vector, a mass-dependent fraction of the binding energy released upon dissociation of:

$$E_1 = \frac{E_B}{1 + m_1/m_2}, \tag{8}$$

where E_B is the binding energy of the parent molecule, m_1 is the molecular mass of the dissociation product of interest, and m_2 is the mass of the partner dissociation product. The direction of the added velocity vector is randomly sampled from a uniform distribution over 4π, with the two dissociation products receiving velocity vectors pointing in opposing directions. Since photo-dissociative ionization reactions that produce additional neutrals are so rare relative to the reactions considered herein, they are neglected altogether as they would not affect the results noticeably.

A.1.2. Sinks

Four possible scenarios can result in the loss of a neutral atom or molecule from the atmosphere in our simulations: (i) gravitational escape, (ii) surface adsorption, (iii) photo- or electron-ionization, and (iv) photo- or electron-dissociation. In the following four paragraphs we present implementation details on each of the four loss processes separately.

Gravitational escape. A particle is said to escape Ganymede's atmosphere when it leaves Ganymede's gravitational attraction. In our simulations, particles reaching the species- and process-specific maximum altitude given in Table 4 are removed from the simulation. The highest maximum altitude of 32,000 km is approximately Ganymede's Hill sphere. For the former two species, the upper boundary is substantially smaller than Ganymede's Hill radius. To ensure that this does not introduce any errors in our results we checked that the number of particles that leave the simulation domain with velocities smaller than the local escape velocity is negligible.

Surface adsorption. Particles that return to the surface either stick to the surface or are re-ejected at the local surface temperature. The species under consideration exhibit vastly different sticking probabilities. Whereas at Ganymede's surface temperature the vapor pressures of O_2 and H_2 are high enough to effectively inhibit condensation, O, H, and OH are chemically so reactive that they effectively always stick (e.g. see Marconi, 2007). H_2O has a highly temperature-dependent vapor pressure (see Fray and Schmitt, 2009), sticking at surface temperatures $\lesssim$150 K but not always, and even when it sticks, it may do so only temporarily, as temperature-dependent residence times down to $\sim$130 K are less than Ganymede's orbital period (e.g., Carberry Mogan et al., 2022; Fig. C.1 therein). H_2O thus sticks in most of the cases, but not always. In our simulations, for H_2O, O_2, and H_2, we make a statistical check against the species' local surface pressure to determine if a returning particles sticks or if it is re-ejected, whereas we remove all returning OH, O, and H particles from the simulation.

Photo- and electron-ionization. Neutral particles are considered lost from Ganymede's atmosphere if they are ionized. In our simulation, ionization happens through an interaction with either a photon or an electron. Ionization as a result of a charge-exchange interaction is also possible, but has not been considered herein. Photo-ionization loss rates at 1 AU have been published by Huebner et al. (1992) and are used herein, after having been propagated to Ganymede's distance from the Sun. Like e.g., Turc et al. (2014), we assume that the exosphere is optically thin so that the photo-loss rates are constant within Ganymede's atmosphere. This is consistent with the way we treat electrons, where we assume that up to the point where an electron encounters an atmospheric particle it has retained its complete energy. Electron-ionization loss rates are much more difficult to quantify, as they depend on the local electron environment and the interaction-specific cross sections. To determine the electron-ionization rates we integrate over the differential electron flux measured by Juno (see Section 2.2) and the energy-dependent reaction cross sections that were provided in literature (see Thompson et al., 1995; Straub et al., 1996; Itikawa and Mason, 2005; McConkey et al., 2008; Deutsch et al., 2014; Joshipura et al., 2017). As mentioned above, two electron populations are modeled in our simulation, and we accordingly compute reaction rates for two different populations. In addition, auroral electrons only have access to the atmosphere within the auroral bands while polar electrons only have access to the atmosphere poleward of the OCFB, as described in Section 2.2. All photo- and electron-ionization loss rates implemented in our model are presented in Table 3.

Photo- and electron-dissociation. Similar to photo- and electron-ionization, we implement photo- and electron-dissociation. The main difference between the two loss processes is that whereas in the first loss process (ionization) the resulting particle (the ion) is considered lost and thus removed from the simulation, the second loss process (dissociation) creates two (or more) new particles (the dissociation products) that are included in the simulation henceforth. These newly created particles start their trajectories at the location where the original molecule is dissociated, with an added energy determined from the molecule's binding energy (see Appendix A.1.1). Similarly to ionization, the photon-dissociation loss rates are taken from Huebner et al. (1992) while the electron-dissociation loss rates are computed by integrating over the energy-dependent electron flux measured by Juno (see Section 2.2) and the energy-dependent electron-dissociation cross sections that have been presented in literature (Itikawa and Mason, 2005; McConkey et al., 2008; Scarlett et al., 2018). Where no cross sections could be found in the literature, the electron impact rates from Ip (1997) and the electron density presented by Carnielli et al. (2019) were used. Again, electron-dissociation only acts in the regions the respective electrons have access to, as described above. Table 3 compiles all photo- and electron-dissociation loss (and source) rates implemented in our simulation.

References

Alday, J., Roth, L., Ivchenko, N., Retherford, K.D., Becker, T.M., Molyneux, P., Saur, J., 2017. New constraints on Ganymede's hydrogen corona: Analysis of Lyman-α emissions observed by HST/STIS between 1998 and 2014. Planet. Space Sci. 148, 35–44. http://dx.doi.org/10.1016/j.pss.2017.10.006.

Allegrini, F., Bagenal, F., Ebert, R.W., Louarn, P., McComas, D.J., Szalay, J.R., Valek, P., Wilson, R., Bolton, S.J., Connerney, J.E.P., Clark, G., Duling, S., Kurth, W.S., Mauk, B., Saur, J., Waite, J.H., 2022. Plasma observations during the 7 June 2021 Ganymede Flyby from the Jovian Auroral distributions experiment (JADE) on Juno. Geophys. Res. Lett. 49 (23), e2022GL098682. http://dx.doi.org/10.1029/2022GL098682.

Allen, R.C., Paranicas, C.P., Bagenal, F., Vines, S.K., Hamilton, D.C., Allegrini, F., Clark, G., Delamere, P.A., Kim, T.K., Krimigis, S.M., Mitchell, D.G., Smith, T.H., Wilson, R.J., 2019. Energetic oxygen and sulfur charge states in the outer Jovian magnetosphere: Insights from the Cassini Jupiter Flyby. Geophys. Res. Lett. 46 (21), 11709–11717. http://dx.doi.org/10.1029/2019GL085185.

Bar-Nun, A., Herman, G., Rappaport, M., Mekler, Y., 1985. Ejection of H_2O, O_2, H_2 and H from water ice by 0.5–6 keV H^+ and Ne^+ ion bombardment. Surf. Sci. 150 (1), 143–156. http://dx.doi.org/10.1016/0039-6028(85)90215-8.

Barabash, S., Brandt, P., Wurz, P., PEP Team, 2016. Particle environment package (PEP) for the ESA JUICE mission. In: AAS/Division for Planetary Sciences Meeting Abstracts #48. In: AAS/Division for Planetary Sciences Meeting Abstracts, vol. 48, p. 422.06.

Barth, C.A., Hord, C.W., Stewart, A.I.F., Pryor, W.R., Simmons, K.E., McClintock, W.E., Ajello, J.M., Naviaux, K.L., Aiello, J.J., 1997. Galileo ultraviolet spectrometer observations of atomic hydrogen in the atmosphere of Ganymede. Geophys. Res. Lett. 24 (17), 2147–2150. http://dx.doi.org/10.1029/97GL01927.

Brown, M.E., Bouchez, A.H., 1999. Observations of Ganymede's visible aurorae. Bull. Am. Astron. Soc. 31, 1183.

Calvin, W.M., Clark, R.N., 1991. Modeling the reflectance spectrum of Callisto 0.25 to 4.1 μm. Icarus 89 (2), 305–317. http://dx.doi.org/10.1016/0019-1035(91)90180-2.

Carberry Mogan, S.R., Tucker, O.J., Johnson, R.E., Roth, L., Alday, J., Vorburger, A., Wurz, P., Galli, A., Smith, H.T., Marchand, B., Oza, A.V., 2022. Callisto's atmosphere: First evidence for H_2 and constraints on H_2O. J. Geophys. Res. (Planets) 127 (11), e2022JE007294. http://dx.doi.org/10.1029/2022JE007294.

Carnielli, G., Galand, M., Leblanc, F., Leclercq, L., Modolo, R., Beth, A., Huybrighs, H.L.F., Jia, X., 2019. First 3D test particle model of Ganymede's ionosphere. Icarus 330, 42–59.

Carnielli, G., Galand, M., Leblanc, F., Modolo, R., Beth, A., Jia, X., 2020a. Constraining Ganymede's neutral and plasma environments through simulations of its ionosphere and Galileo observations. Icarus 113691.

Carnielli, G., Galand, M., Leblanc, F., Modolo, R., Beth, A., Jia, X., 2020b. Simulations of ion sputtering at Ganymede. Icarus 351, 113918.

Cassidy, T., Coll, P., Raulin, F., Carlson, R., Johnson, R., Loeffler, M., Hand, K., Baragiola, R., 2010. Radiolysis and Photolysis of Icy Satellite Surfaces: Experiments and Theory. Space Sci. Rev. 153, 299–315. http://dx.doi.org/10.1007/s11214-009-9625-3.

Clark, G., Kollmann, P., Mauk, B.H., Paranicas, C., Haggerty, D., Rymer, A., Smith, H.T., Saur, J., Allegrini, F., Duling, S., Ebert, R.W., Kurth, W.S., Gladstone, R., Greathouse, T.K., Li, W., Bagenal, F., Connerney, J.E.P., Bolton, S., Szalay, J.R., Sulaiman, A.H., Hansen, C.J., Turner, D.L., 2022. Energetic charged particle observations during Juno's close flyby of Ganymede. Geophys. Res. Lett. 49 (23), e2022GL098572. http://dx.doi.org/10.1029/2022GL098572.

Clark, G., Mauk, B.H., Kollmann, P., Paranicas, C., Bagenal, F., Allen, R.C., Bingham, S., Bolton, S., Cohen, I., Ebert, R.W., Dunn, W., Haggerty, D., Houston, S.J., Jackman, C.M., Roussos, E., Rymer, A., Westlake, J.H., 2020. Heavy ion charge states in Jupiter's Polar magnetosphere inferred from auroral megavolt electric potentials. J. Geophys. Res. Space Phys. 125 (9), e2020JA028052. http://dx.doi.org/10.1029/2020JA028052.

Clark, R.N., McCord, T.B., 1980. The Galilean satellites: New near-infrared spectral reflectance measurements (0.65-2.5 μm) and a 0.325-5 μm summary. Icarus 41 (3), 323–339. http://dx.doi.org/10.1016/0019-1035(80)90217-1.

Davis, M.R., Meier, R.M., Cooper, J.F., Loeffler, M.J., 2021. The contribution of electrons to the sputter-produced O_2 exosphere on Europa. Astrophys. J. Lett. 908 (2), L53. http://dx.doi.org/10.3847/2041-8213/abe415.

de Kleer, K., Milby, Z., Schmidt, C., Camarca, M., Brown, M.E., 2023. The optical aurorae of europa, ganymede, and callisto. Planet. Sci. J. 4 (2), 37. http://dx.doi.org/10.3847/PSJ/acb53c.

Deutsch, H., Bronold, F., Becker, K., 2014. Calculation of electron-impact ionization cross sections: Bottom-up inductive vs. top-down deductive approaches. Int. J. Mass Spectrom. 365–366, 128–139. http://dx.doi.org/10.1016/j.ijms.2014.01.011.

Duling, S., Saur, J., Clark, G., Allegrini, F., Greathouse, T., Gladstone, R., Kurth, W., Connerney, J.E.P., Bagenal, F., Sulaiman, A.H., 2022. Ganymede MHD model: Magnetospheric context for Juno's PJ34 flyby. Geophys. Res. Lett. 49 (24), e2022GL101688. http://dx.doi.org/10.1029/2022GL101688.

Ebert, R.W., Fuselier, S.A., Allegrini, F., Bagenal, F., Bolton, S.J., Clark, G., Connerney, J.E.P., DiBraccio, G.A., Kurth, W.S., Levin, S., McComas, D.J., Montgomery, J., Romanelli, N., Sulaiman, A.H., Szalay, J.R., Valek, P., Wilson, R.J., 2022. Evidence for magnetic reconnection at Ganymede's upstream magnetopause during the PJ34 Juno flyby. Geophys. Res. Lett. 49 (23), http://dx.doi.org/10.1029/2022GL099775.

Eviatar, A., Strobel, D.F., Wolven, B.C., Feldman, P.D., McGrath, M.A., Williams, D.J., 2001. Excitation of the Ganymede ultraviolet aurora. Astrophys. J. 555 (2), 1013–1019. http://dx.doi.org/10.1086/321510.

Famá, M., Shi, J., Baragiola, R.A., 2008. Sputtering of ice by low-energy ions. Surf. Sci. 602, 156–161. http://dx.doi.org/10.1016/j.susc.2007.10.002.

Fatemi, S., Poppe, A.R., Khurana, K.K., Holmström, M., Delory, G.T., 2016. On the formation of Ganymede's surface brightness asymmetries: Kinetic simulations of Ganymede's magnetosphere. Geophys. Res. Lett. 43 (10), 4745–4754. http://dx.doi.org/10.1002/2016GL068363.

Feldman, P.D., McGrath, M.A., Strobel, D.F., Moos, H.W., Retherford, K.D., Wolven, B.C., 2000. HST/STIS ultraviolet imaging of polar aurora on Ganymede. Astrophys. J. 535 (2), 1085–1090. http://dx.doi.org/10.1086/308889.

Fray, N., Schmitt, B., 2009. Sublimation of ices of astrophysical interest: A bibliographic review. Planet. Space Sci. 57, 2053–2080. http://dx.doi.org/10.1016/j.pss.2009.09.011.

Galli, A., Vorburger, A., Carberry Mogan, S.R., Roussos, E., Stenberg Wieser, G., Wurz, P., Föhn, M., Krupp, N., Fränz, M., Barabash, S., Futaana, Y., Brandt, P.C., Kollmann, P., Haggerty, D.K., Jones, G.H., Johnson, R.E., Tucker, O.J., Simon, S., Tippens, T., Liuzzo, L., 2022. Callisto's atmosphere and its space environment: Prospects for the particle environment package on board JUICE. Earth Space Sci. 9 (5), e2021EA002172. http://dx.doi.org/10.1029/2021EA002172.

Galli, A., Vorburger, A., Wurz, P., Cerubini, R., Tulej, M., 2018. First experimental data of sulphur ions sputtering water ice. Icarus 312, 1–6. http://dx.doi.org/10.1016/j.icarus.2018.04.029.

Galli, A., Vorburger, A., Wurz, P., Galand, M., Oza, A., Fatemi, S., Plainaki, C., Mura, A., 2023. Interactions between the space environment and Ganymede's surface. In: Ganymede. Cambridge University Press, Cambridge.

Galli, A., Vorburger, A., Wurz, P., Pommerol, A., Cerubini, R., Jost, B., Poch, O., Tulej, M., Thomas, N., 2018. 0.2 To 10 keV electrons interacting with water ice: Radiolysis, sputtering, and sublimation. Planet. Space Sci. 155, 91–98. http://dx.doi.org/10.1016/j.pss.2017.11.016.

Galli, A., Vorburger, A., Wurz, P., Tulej, M., 2017. Sputtering of water ice films: A re-assessment with singly and doubly charged oxygen and argon ions, molecular oxygen, and electrons. Icarus 291, 36–45. http://dx.doi.org/10.1016/j.icarus.2017.03.018.

Greathouse, T.K., Gladstone, G.R., Molyneux, P.M., Versteeg, M.H., Hue, V., Kammer, J.A., Davis, M.W., Bolton, S.J., Giles, R.S., Connerney, J.E.P., Gerard, J.-C., Grodent, D.C., Bonfond, B., Saur, J., Duling, S., 2022. UVS observations of Ganymede's aurora during juno orbits 34 and 35. Geophys. Res. Lett. 49 (23), e2022GL099794. http://dx.doi.org/10.1029/2022GL099794.

Grieves, G.A., Orlando, T.M., 2005. The importance of pores in the electron stimulated production of D2 and O2 in low temperature ice. Surf. Sci. 593 (1), 180–186. http://dx.doi.org/10.1016/j.susc.2005.06.059.

Gurnett, D.A., Kurth, W.S., Roux, A., Bolton, S.J., Kennel, C.F., 1996. Evidence for a magnetosphere at Ganymede from plasma-wave observations by the Galileo spacecraft. Nature 384, 535–537.

Hall, D.T., Feldman, P.D., McGrath, M.A., Strobel, D.F., 1998. The far-ultraviolet oxygen airglow of Europa and Ganymede. Astrophys. J. 499 (1), 475–481. http://dx.doi.org/10.1086/305604.

Hansen, C.J., Bolton, S., Sulaiman, A.H., Duling, S., Bagenal, F., Brennan, M., Connerney, J., Clark, G., Lunine, J., Levin, S., Kurth, W., Mura, A., Paranicas, C., Tosi, F., Withers, P., 2022. Juno's close encounter with Ganymede—An overview. Geophys. Res. Lett. 49 (23), e2022GL099285. http://dx.doi.org/10.1029/2022GL099285.

Hansen, G.B., McCord, T.B., 2004. Amorphous and crystalline ice on the Galilean satellites: A balance between thermal and radiolytic processes. J. Geophys. Res.: Planets 109 (E1), http://dx.doi.org/10.1029/2003JE002149.

Huebner, W.F., Keady, J.J., Lyon, S.P., 1992. Solar photo rates for planetary atmospheres and atmospheric pollutants. Astrophys. Space Sci. 195 (1), 1–294. http://dx.doi.org/10.1007/BF00644558.

Ip, W.H., 1997. On the neutral cloud distribution in the Saturnian magnetosphere. Icarus 126 (1), 42–57. http://dx.doi.org/10.1006/icar.1996.5618.

Itikawa, Y., Mason, N., 2005. Cross sections for electron collisions with water molecules. J. Phys. Chem. Ref. Data 34 (1), 1–22. http://dx.doi.org/10.1063/1.1799251.

Johnson, R.E., Burger, M.H., Cassidy, T.A., Leblanc, F., Marconi, M., Smyth, W.H., 2009. Composition and detection of Europa's sputter-induced atmosphere. In: Pappalardo, R.T., McKinnon, W.B., Khurana, K.K. (Eds.), Europa. University of Arizona Press, p. 507.

Johnson, R.E., Carlson, R.W., Cassidy, T.A., Fama, M., 2013. Sputtering of ices. In: Gudipati, M.S., Castillo-Rogez, J. (Eds.), The Science of Solar System Ices. Springer New York, New York, NY, pp. 551–581. http://dx.doi.org/10.1007/978-1-4614-3076-6_17.

Johnson, R., Leblanc, F., Yakshinskiy, B., Madey, T., 2002. Energy distributions for desorption of sodium and potassium from ice: The Na/K ratio at Europa. Icarus 156 (1), 136–142. http://dx.doi.org/10.1006/icar.2001.6763.

Johnson, R., Liu, M., 1996. Molecular dynamics studies of minicascades in electronically stimulated sputtering of condensed-gas solids. J. Chem. Phys. 104, 6041–6051.

Joshipura, K.N., Pandya, S.H., Mason, N.J., 2017. Electron scattering and ionization of H_2O; OH, H_2O_2, HO_2 radicals and $(H_2O)_2$ dimer. Eur. Phys. J. D 71 (4), 96. http://dx.doi.org/10.1140/epjd/e2017-70510-7.

Kersten, E., Zubarev, A., Roatsch, T., Matz, K.-D., 2021. Controlled global Ganymede mosaic from Voyager and Galileo images. Planet. Space Sci. 206, 105310. http://dx.doi.org/10.1016/j.pss.2021.105310.

Kim, T.K., Ebert, R.W., Valek, P.W., Allegrini, F., McComas, D.J., Bagenal, F., Chae, K., Livadiotis, G., Loeffler, C.E., Pollock, C., Ranquist, D.A., Thomsen, M.F., Wilson, R.J., Clark, G., Kollmann, P., Mauk, B.H., Bolton, S., Levin, S., Nicolaou, G., 2020. Method to derive ion properties from Juno JADE including abundance estimates for O+ and S2+. J. Geophys. Res. Space Phys. 125 (2), e2018JA026169. http://dx.doi.org/10.1029/2018JA026169.

Kivelson, M.G., Bagenal, F., Kurth, W.S., Neubauer, F.M., Paranicas, C., Saur, J., 2004. Magnetospheric interactions with satellites. In: Bagenal, F., Dowling, T.E., McKinnon, W.B. (Eds.), In: Jupiter. The Planet, Satellites and Magnetosphere, vol. 1, Cambridge University Press, pp. 513–536.

Kivelson, M.G., Khurana, K.K., Volwerk, M., 2002. The permanent and inductive magnetic moments of Ganymede. Icarus 157 (2), 507–522.

Kurth, W.S., Sulaiman, A.H., Hospodarsky, G.B., Menietti, J.D., Mauk, B.H., Clark, G., Allegrini, F., Valek, P., Connerney, J.E.P., Waite, J.H., Bolton, S.J., Imai, M., Santolik, O., Li, W., Duling, S., Saur, J., Louis, C., 2022. Juno plasma wave observations at Ganymede. Geophys. Res. Lett. 49 (23), e2022GL098591. http://dx.doi.org/10.1029/2022GL098591.

Leblanc, F., Oza, A., Leclercq, L., Schmidt, C., Cassidy, T., Modolo, R., Chaufray, J., Johnson, R., 2017. On the orbital variability of Ganymede's atmosphere. Icarus 293, 185–198. http://dx.doi.org/10.1016/j.icarus.2017.04.025.

Leblanc, F., Roth, L., Chaufray, J., Modolo, R., Galand, M., Ivchenko, N., Carnielli, G., Baskevitch, C., Oza, A., Werner, A., 2023. Ganymede's atmosphere as constrained by HST/STIS observations. Icarus 399, 115557. http://dx.doi.org/10.1016/j.icarus.2023.115557.

Ligier, N., Paranicas, C., Carter, J., Poulet, F., Calvin, W., Nordheim, T., Snodgrass, C., Ferellec, L., 2019. Surface composition and properties of Ganymede: Updates from ground-based observations with the near-infrared imaging spectrometer SINFONI/VLT/ESO. Icarus 333, 496–515. http://dx.doi.org/10.1016/j.icarus.2019.06.013.

Liuzzo, L., Poppe, A.R., Paranicas, C., Nénon, Q., Fatemi, S., Simon, S., 2020. Variability in the energetic electron bombardment of Ganymede. J. Geophys. Res. Space Phys. 1–35. http://dx.doi.org/10.1029/2020JA028347.

Loeffler, M.J., Teolis, B.D., Baragiola, R.A., 2006. A model study of the thermal evolution of astrophysical ices. Astrophys. J. 639 (2), L103–L106. http://dx.doi.org/10.1086/502969.

Marconi, M., 2007. A kinetic model of Ganymede's atmosphere. Icarus 190 (1), 155–174. http://dx.doi.org/10.1016/j.icarus.2007.02.016.

Marzok, A., Schlegel, S., Saur, J., Roth, L., Grodent, D., Strobel, D.F., Retherford, K.D., 2022. Mapping the brightness of Ganymede's ultraviolet aurora using hubble space telescope observations. J. Geophys. Res.: Planets 127 (6), e2022JE007256. http://dx.doi.org/10.1029/2022JE007256.

McConkey, J.W., Malone, C.P., Johnson, P.V., Winstead, C., McKoy, V., Kanik, I., 2008. Electron impact dissociation of oxygen-containing molecules A critical review. Phys. Rep. 466 (1–3), 1–103. http://dx.doi.org/10.1016/j.physrep.2008.05.001.

McGrath, M.A., Jia, X., Retherford, K., Feldman, P.D., Strobel, D.F., Saur, J., 2013. Aurora on Ganymede. J. Geophys. Res. (Space Physics) 118 (5), 2043–2054. http://dx.doi.org/10.1002/jgra.50122.

McGrath, M.A., Lellouch, E., Strobel, D.F., Feldman, P.D., Johnson, R.E., 2004. Satellite atmospheres. In: Bagenal, F., Dowling, T.E., McKinnon, W.B. (Eds.), Jupiter. the Planet, Satellites and Magnetosphere. Cambridge University Press, pp. 457–483.

Molyneux, P., Nichols, J., Bannister, N., Bunce, E., Clarke, J., Cowley, S., Gérard, J., Grodent, D., Milan, S., Paty, C., 2017. Hubble space telescope observations of hemispheric and temporal variations in Ganymede's oxygen atmosphere and aurora. In: Magnetospheres of the Outer Planets Conference.

Molyneux, P.M., Nichols, J.D., Bannister, N.P., Bunce, E.J., Clarke, J.T., Cowley, S.W.H., Gérard, J.C., Grodent, D., Milan, S.E., Paty, C., 2018. Hubble space telescope observations of variations in Ganymede's oxygen atmosphere and aurora. J. Geophys. Res. (Space Physics) 123 (5), 3777–3793. http://dx.doi.org/10.1029/2018JA025243.

Moore, J.M., Chapman, C.R., Bierhaus, E.B., Greeley, R., Chuang, F.C., Klemaszewski, J., Clark, R.N., Dalton, J.B., Hibbitts, C.A., Schenk, P.M., Spencer, J.R., Wagner, R., 2004. Callisto. In: Bagenal, F., Dowling, T.E., McKinnon, W.B. (Eds.), In: Jupiter. the Planet, Satellites and Magnetosphere, vol. 1, Callisto, Cambridge University Press, pp. 397–426.

Musacchio, F., Saur, J., Roth, L., Retherford, K.D., McGrath, M.A., Feldman, P.D., Strobel, D.F., 2017. Morphology of Ganymede's FUV auroral ovals. J. Geophys. Res. (Space Physics) 122 (3), 2855–2876. http://dx.doi.org/10.1002/2016JA023220.

Noll, K.S., Johnson, R.E., Lane, A.L., Domingue, D.L., Weaver, H.A., 1996. Detection of ozone on Ganymede. Science 273 (5273), 341–343. http://dx.doi.org/10.1126/science.273.5273.341.

Orton, G.S., Spencer, J.R., Travis, L.D., Martin, T.Z., Tamppari, L.K., 1996. Galileo photopolarimeter-radiometer observations of Jupiter and the Galilean satellites. Science 274 (5286), 389–391. http://dx.doi.org/10.1126/science.274.5286.389.

Pilcher, C.B., Ridgway, S.T., McCord, T.B., 1972. Galilean satellites: Identification of water frost. Science 178 (4065), 1087–1089. http://dx.doi.org/10.1126/science.178.4065.1087.

Plainaki, C., Massetti, S., Jia, X., Mura, A., Milillo, A., Grassi, D., Sindoni, G., D'Aversa, E., Filacchione, G., 2020. Kinetic simulations of the Jovian energetic ion circulation around Ganymede. Astrophys. J. 900 (1), 74.

Plainaki, C., Milillo, A., Massetti, S., Mura, A., Jia, X., Orsini, S., Mangano, V., De Angelis, E., Rispoli, R., 2015. The H2O and O2 exospheres of Ganymede: The result of a complex interaction between the jovian magnetospheric ions and the icy moon. Icarus 245, 306–319. http://dx.doi.org/10.1016/j.icarus.2014.09.018.

Poppe, A.R., Fatemi, S., Khurana, K.K., 2018. Thermal and energetic ion dynamics in Ganymede's magnetosphere. J. Geophys. Res. Space Phys. 123 (6), 4614–4637. http://dx.doi.org/10.1029/2018JA025312.

Reimann, C., Boring, J., Johnson, R., Garrett, J., Farmer, K., Brown, W., Marcantonio, K., Augustyniak, W., 1984. Ion-induced molecular ejection from D_2O ice. Surf. Sci. 147 (1), 227–240. http://dx.doi.org/10.1016/0039-6028(84)90177-8.

Roederer, J.G., Zhang, H., 2014. Dynamics of Magnetically Trapped Particles. Springer Berlin, Heidelberg, http://dx.doi.org/10.1007/978-3-642-41530-2.

Romanelli, N., DiBraccio, G.A., Modolo, R., Connerney, J.E.P., Ebert, R.W., Martos, Y.M., Weber, T., Espley, J.R., Kurth, W.S., Allegrini, F., Valek, P., Bolton, S.J., 2022. Juno magnetometer observations at Ganymede: Comparisons with a global hybrid simulation and indications of magnetopause reconnection. Geophys. Res. Lett. 49 (23), e2022GL099545. http://dx.doi.org/10.1029/2022GL099545.

Roth, L., Ivchenko, N., Gladstone, G.R., Saur, J., Grodent, D., Bonfond, B., Molyneux, P.M., Retherford, K.D., 2021. Evidence for a sublimated water atmosphere on Ganymede from Hubble space telescope observations. arXiv e-prints arXiv:2106.03570.

Roth, L., Marchesini, G., Becker, T.M., Hoeijmakers, H.J., Molyneux, P.M., Retherford, K.D., Saur, J., Mogan, S.R.C., Szalay, J.R., 2023. Probing Ganymede's atmosphere with HST Lyα images in transit of Jupiter. Planet. Sci. J. 4 (1), 12. http://dx.doi.org/10.3847/PSJ/acaf7f.

Saur, J., Duling, S., Roth, L., Jia, X., Strobel, D.F., Feldman, P.D., Christensen, U.R., Retherford, K.D., McGrath, M.A., Musacchio, F., Wennmacher, A., Neubauer, F.M., Simon, S., Hartkorn, O., 2015. The search for a subsurface ocean in Ganymede with Hubble space telescope observations of its auroral ovals. J. Geophys. Res. (Space Physics) 120 (3), 1715–1737. http://dx.doi.org/10.1002/2014JA020778.

Saur, J., Duling, S., Wennmacher, A., Willmes, C., Roth, L., Strobel, D.F., Allegrini, F., Bagenal, F., Bolton, S.J., Bonfond, B., Clark, G., Gladstone, R., Greathouse, T.K., Grodent, D.C., Hansen, C.J., Kurth, W.S., Orton, G.S., Retherford, K.D., Rymer, A.M., Sulaiman, A.H., 2022. Alternating north-south brightness ratio of Ganymede's auroral ovals: Hubble space telescope observations around the Juno PJ34 flyby. Geophys. Res. Lett. 49 (23), e2022GL098600. http://dx.doi.org/10.1029/2022GL098600.

Scarlett, L.H., Tapley, J.K., Fursa, D.V., Zammit, M.C., Savage, J.S., Bray, I., 2018. Electron-impact dissociation of molecular hydrogen into neutral fragments. Eur. Phys. J. D 72 (2), 34. http://dx.doi.org/10.1140/epjd/e2017-80649-8.

Shematovich, V.I., 2016. Neutral atmosphere near the icy surface of Jupiter's moon Ganymede. Solar Syst. Res. 50 (4), 262–280. http://dx.doi.org/10.1134/S0038094616040067.

Showman, A.P., Malhotra, R., 1999. The Galilean satellites. Science 286 (5437), 77–84. http://dx.doi.org/10.1126/science.286.5437.77.

Sigmund, P., 1981. Sputtering by ion bombardment theoretical concepts. In: Behrisch, R. (Ed.), Sputtering By Particle Bombardment I: Physical Sputtering of Single-Element Solids. Springer Berlin Heidelberg, Berlin, Heidelberg, pp. 9–71. http://dx.doi.org/10.1007/3540105212_7.

Spencer, J.R., 1987. Icy Galilean satellite reflectance spectra: Less ice on Ganymede and Callisto? Icarus 70 (1), 99–110. http://dx.doi.org/10.1016/0019-1035(87)90077-7.

Spencer, J.R., Calvin, W.M., Person, M.J., 1995. CCD spectra of the Galilean satellites: Molecular oxygen on Ganymede. J. Geophys. Res. 100 (E9), 19049–19056. http://dx.doi.org/10.1029/95JE01503.

Straub, H.C., Renault, P., Lindsay, B.G., Smith, K.A., Stebbings, R.F., 1996. Absolute partial cross sections for electron-impact ionization of H_2, N_2, and O_2 from threshold to 1000 eV. Phys. Rev. A 54 (3), 2146–2153. http://dx.doi.org/10.1103/PhysRevA.54.2146.

Szalay, J.R., Smith, H.T., Zirnstein, E.J., McComas, D.J., Begley, L.J., Bagenal, F., Delamere, P.A., Wilson, R.J., Valek, P.W., Poppe, A.R., Nénon, Q., Allegrini, F., Ebert, R.W., Bolton, S.J., 2022. Water-group pickup ions from Europa-Genic neutrals orbiting Jupiter. Geophys. Res. Lett. 49 (9), e2022GL098111. http://dx.doi.org/10.1029/2022GL098111.

Teolis, B.D., Plainaki, C., Cassidy, T.A., Raut, U., 2017. Water ice radiolytic O_2, H_2, and H_2O_2 yields for any projectile species, energy, or temperature: A model for icy astrophysical bodies. J. Geophys. Res.: Planets 122 (10), 1996–2012. http://dx.doi.org/10.1002/2017JE005285.

Thompson, W.R., Shah, M.B., Gilbody, H.B., 1995. Single and double ionization of atomic oxygen by electron impact. J. Phys. B: At. Mol. Opt. Phys. 28 (7), 1321–1330. http://dx.doi.org/10.1088/0953-4075/28/7/023.

Turc, L., Leclercq, L., Leblanc, F., Modolo, R., Chaufray, J.-Y., 2014. Modelling Ganymede's neutral environment: A 3D test-particle simulation. Icarus 229, 157–169. http://dx.doi.org/10.1016/j.icarus.2013.11.005.

Vorburger, A., Fatemi, S., Galli, A., Liuzzo, L., Poppe, A.R., Wurz, P., 2022. 3D Monte-Carlo simulation of Ganymede's water exosphere. Icarus 375, 114810. http://dx.doi.org/10.1016/j.icarus.2021.114810.

Vorburger, A., Pfleger, M., Lindkvist, J., Holmström, M., Lammer, H., Lichtenegger, H.I.M., Galli, A., Rubin, M., Wurz, P., 2019. Three-dimensional modeling of Callisto's surface sputtered exosphere environment. J. Geophys. Res. (Space Physics) 124 (8), 7157–7169. http://dx.doi.org/10.1029/2019JA026610.

Vorburger, A., Wurz, P., 2018. Europa's ice-related atmosphere: The sputter contribution. Icarus 311, 135–145. http://dx.doi.org/10.1016/j.icarus.2018.03.022.

Vorburger, A., Wurz, P., 2021. Modeling of possible plume mechanisms on Europa. J. Geophys. Res. Space Phys. 126 (9), e2021JA029690. http://dx.doi.org/10.1029/2021JA029690.

Vorburger, A., Wurz, P., Lammer, H., Barabash, S., Mousis, O., 2015. Monte-Carlo simulation of Callisto's exosphere. Icarus 262, 14–29. http://dx.doi.org/10.1016/j.icarus.2015.07.035.

Zheng, W., Jewitt, D., Kaiser, R.I., 2006. Formation of hydrogen, oxygen, and hydrogen peroxide in electron-irradiated crystalline water ice. Astrophys. J. 639 (1), 534–548. http://dx.doi.org/10.1086/499231.